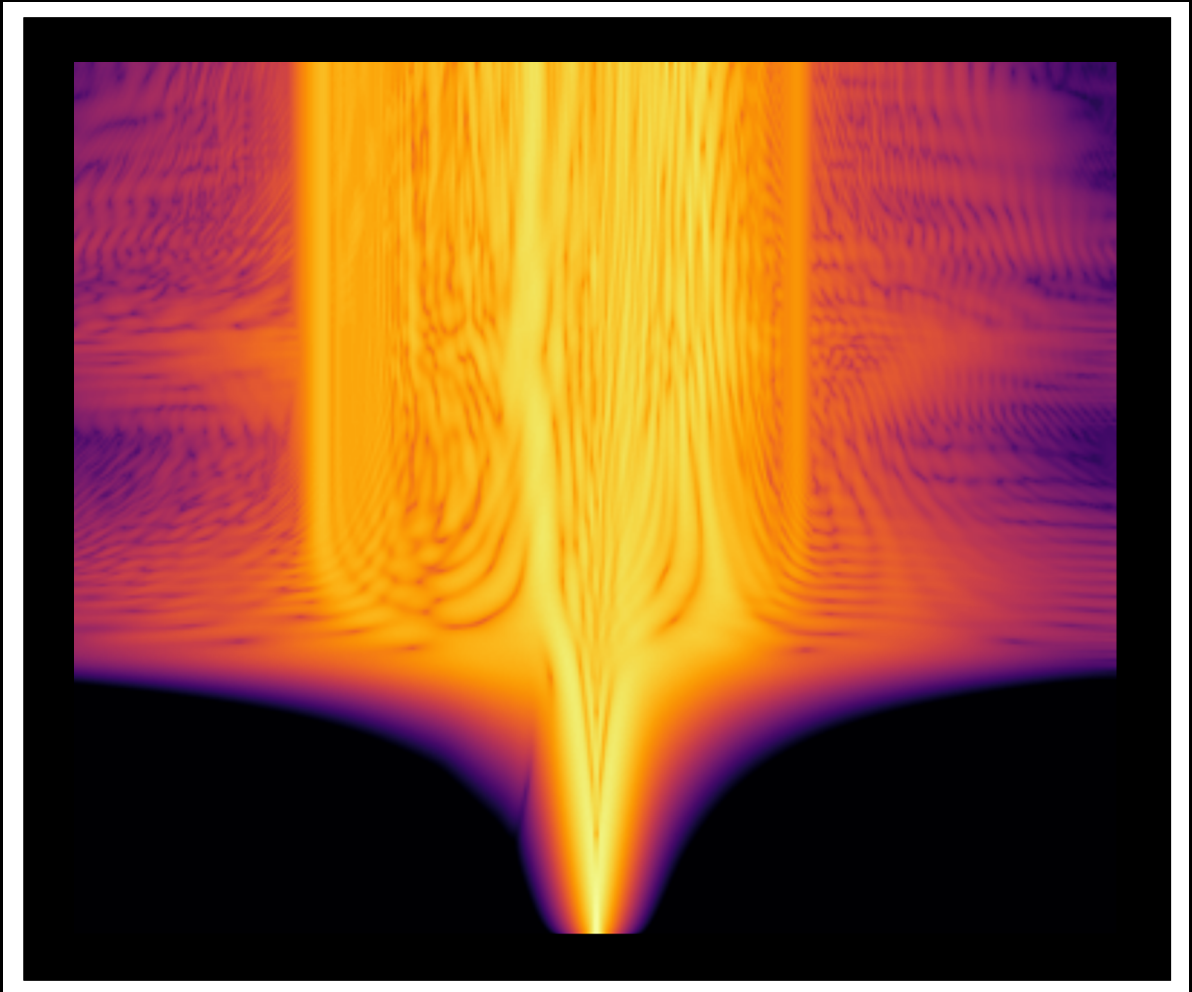


Modelling nonlinear optical
pulse propagation
using pseudo-spectral methods



Bas Schuttrups

Master's thesis

Applied Physics & Applied Mathematics

Modelling nonlinear optical pulse propagation using pseudo-spectral methods

by Bas Schuttrups

Master's Thesis

Applied Physics & Applied Mathematics

Enschede, September 2020

Supervisors

Prof. Dr. Ir. B.J. Geurts (MMS)

Dr. P.J.M. van der Slot (LPNO)

Graduation committee

Prof. Dr. K.-J. Boller (LPNO)

Dr. C. Brune (Applied Analysis)

Prof. Dr. Ir. B.J. Geurts (MMS)

Dr. Ir. H.L. Offerhaus (Optical Sciences)

Dr. P.J.M. van der Slot (LPNO)

This work was done at the following research groups

Laser Physics & Nonlinear Optics (LPNO) Multiscale Modelling & Simulation (MMS)

Mesa+ Institute for Nanotechnology

Faculty of Electrical Engineering,

Faculty of Science & Technology

Mathematics & Computer Science

University of Twente

P.O. Box 217

7500 AE Enschede, the Netherlands

Abstract

We present a newly developed code for simulating nonlinear pulse propagation in waveguides, using the efficient fourth-order Runge-Kutta method in the interaction picture (RK4IP). We compare RK4IP with the widely-used split-step Fourier method (SSFM) for solving both the normal and generalised nonlinear Schrödinger equation. We provide verification and validation for our results and confirm 2nd- and 4th-order convergence for SSFM and RK4IP, respectively. In addition, we find that RK4IP is a more accurate and computationally efficient method than SSFM, especially for simulating more complex and highly dynamic cases. We use RK4IP to study the nonlinear propagation and asymptotic behaviour of various optical pulses. Finally, we present the results of simulating supercontinuum generation in a photonic crystal fiber. Our simulation results show the increase of spectral broadening as the pulse energy increases, while keeping a constant input pulse width of 60 fs. We find the generation of a supercontinuum with a maximum spectral width of 547 THz for the maximum input pulse energy of 501 pJ.

Contents

1	Introduction	4
2	Theory of nonlinear pulse propagation	7
2.1	Nonlinear Schrödinger Equation	8
2.1.1	Derivation of the nonlinear Schrödinger equation	8
2.1.2	Dimensionless form	11
2.1.3	Self-phase modulation & soliton solutions	12
2.2	Generalised Nonlinear Schrödinger Equation	15
2.2.1	Fundamental soliton and third-order dispersion	16
2.2.2	Soliton fission	17
2.2.3	Dispersive waves	17
3	Numerical methods	20
3.1	Notation	21
3.2	Split-Step Methods	22
3.3	RK4IP Method	25
3.4	Measure of convergence	26
3.4.1	Relative error	27
3.4.2	Relative difference	28
4	Predicting nonlinear pulse propagation	30
4.1	Nonlinear Schrödinger Equation	30
4.1.1	Pulse propagation	31
4.1.2	Convergence with respect to analytical solutions	36
4.2	Generalised Nonlinear Schrödinger Equation	38
4.2.1	Material properties	38
4.2.2	Comparison of results with theory	39
4.2.3	Convergence of numerical solutions	42
4.2.4	Determining suitable numerical parameters	43
4.2.5	Simulation of supercontinuum generation	44
5	Conclusions & outlook	49
5.1	Outlook	50
	References	52
A	Modelling Kerr frequency comb generation	57
A.1	Lugiato-Lefever Equation	57
A.1.1	Dimensionless form	59
A.2	Steady state, spatially uniform solutions	59

Chapter 1

Introduction

The field of nonlinear optics studies the interaction of light with materials, for which the response to an optical field depends in a nonlinear fashion on the strength of the optical field. This means that the optical response of such a material cannot be expressed as a linear function of the field, but rather requires a nonlinear one. This nonlinear response then emerges in the constitutive relations used in Maxwell's equations, turning them into a set of nonlinear equations. The study of nonlinear optics has existed for more than a century, ever since Kerr showed [40] that birefringence¹ can be induced in an otherwise isotropic medium by applying a dc electric field to the medium [10]. The various nonlinear processes are typically ordered by the integer order of the nonlinearity [12], the lowest nonlinear order being the second order. The optical waveguiding systems considered in this work are comprised of amorphous glasses. Such materials are centro-symmetric and therefore do not possess a bulk second-order nonlinearity. For these materials, the first non-zero nonlinearity is the third order, which gives rise to self-steepening, Raman-scattering and the *nonlinear Kerr effect*. This Kerr effect is the nonlinearity that is behind Kerr's discovery and it is the nonlinearity we are focussing on in this work.

The nonlinear behaviour of materials has the inherent feature that it can lead to the generation of new frequency components not initially present in the optical field. This effect of nonlinear behaviour can be used to obtain spectral broadening of light. In particular, it is called *supercontinuum generation* (SCG) when relatively narrowband pulses undergo extreme spectral broadening due to nonlinear effects to yield broadband, spectrally continuous pulses. Such broadband pulses have found application in, among others, optical coherence tomography, IR microscopy [19], fluorescence lifetime imaging microscopy, Förster resonance energy transfer, scanning laser ophthalmology, flow cytometry or super-resolution techniques such as stimulated emission depletion microscopy [28]. Broadband pulses can be used in combination with tunable spectral filters to create a versatile laser tool, suitable

¹Birefringence is an anisotropic effect in which the refractive index of a material depends on the polarisation and propagation direction of the light.

for many applications [28]. SCG was first reported in 1970 in bulk glass [6, 7], but has been especially successful since the advent of photonic crystal fiber waveguides [18]. More recently, SCG has also been successfully demonstrated in waveguides on-chip through the use of integrated optics [44, 22]. This allows for integration of components that use SCG with other integrated optics technologies. Additionally, an integrated optics-approach comes with the possibility of mass production, which has major technological, economical and environmental benefits. The process of extreme spectral broadening has also been used in microring resonators to generate so-called Kerr frequency combs [15]. Such frequency combs have applications in, among others, metrology [32], optical telecommunication [47] and dual-comb spectroscopy [54].

The nonlinear propagation of pulses through waveguides, be it in a fiber or in an integrated waveguide, was first modelled by the *nonlinear Schrödinger equation* (NLSE) [39], which describes how group velocity dispersion and the Kerr effect influence pulse propagation. The more elaborate *Generalised NLSE* (GNLSE) also models loss, higher-order dispersion and other third-order nonlinear effects, such as Raman scattering, spontaneous Raman noise and self-steepening. These third-order nonlinear effects give rise to a number of interesting features for the propagation of pulses in waveguides, such as self-phase modulation, formation of optical shock-waves and the formation and break-up of so-called soliton pulses. Soliton pulses are pulses that are shaped such that they balance the nonlinear and dispersive effects of the medium they are travelling in, allowing them to propagate either without changing their shape or changing their shape in a periodic fashion. These were first observed in the study of shallow-water waves and were called solitary waves [4]. The term *soliton* was first used in a paper about numerical solutions of the Korteweg-deVries equation (KdV), the equation that models shallow-water waves, to reflect their particle-like nature [59]. This discovery was soon followed by the introduction of the inverse scattering transform [26, 25], a method for solving nonlinear PDEs like the KdV, e.g., the Gross-Pitaevskii equation for the dynamics of Bose-Einstein condensates [13]. This method was later used to show that optical solitons form a set of analytical solutions to the (G)NLSE [50]. Soliton pulses play a large role in the dynamics of SCG. In addition, they are a set of reference solutions that can be used for the validation of numerical solutions to the (G)NLSE.

The highly dynamic nature of nonlinear pulse propagation in both waveguides and microrings, means that the GNLSE does not have any known analytical solutions. Only for very particular cases, e.g., for which the GNLSE reduces to the NLSE, are some analytical solutions, such as solitons, known. Therefore, we need numerical modelling in order to thoroughly understand the dynamics of nonlinear pulse propagation and to be able to engineer the waveguide to tailor certain characteristics of the supercontinuum generated. Additionally, numerical modelling allows us to study the effect of including or excluding various processes. Also, it allows us to study nonlinear pulse propagation in the time domain, where experimental data can typically only be obtained in the frequency domain at the output of the waveguide. Numerical modelling involves the use of numerical methods to solve either the NLSE or the GNLSE. Many methods have been used

for this purpose [55], one of them being the split-step Fourier method (SSFM) [23]. SSFM has been the most commonly used method to solve equations like the NLSE [4], including the nonlinear propagation of light in microring resonators. However, more methods have been proposed throughout the years, one of them being the *fourth-order Runge-Kutta method in the interaction picture* (RK4IP), a more efficient method based on the widely popular RK4 integration method [36]. RK4IP has been used to solve the GNLSE for some years now.

In this report, we present a newly developed code in Python for simulating nonlinear pulse propagation in waveguides, following the approach from Hult [36]. We study the dynamics of nonlinear pulse propagation by employing both SSFM and RK4IP for solving both the NLSE and the GNLSE. Furthermore, we aim to extend the use of RK4IP from simulating pulse propagation in waveguides to microring resonators as well, to allow modelling of Kerr frequency comb generation, in addition to SCG.

In chapter 2, we give a detailed overview of the theory of nonlinear pulse propagation. We summarise the derivation that converts Maxwell's equations into the NLSE and treat some of the theoretical properties of both the NLSE and the GNLSE. In Chapter 3, we describe SSFM and RK4IP in detail and consider their properties, such as order of convergence and efficiency. In addition, we provide some methods for quantitatively analysing numerical results. In chapter 4, we present our results from solving the NLSE and the GNLSE with the two methods mentioned. We verify our implementation by showing convergence of results w.r.t. various parameters and by checking that the order of convergence of our implementation agrees with what we theoretically expect. In addition, we validate the correctness of our results by comparing them with theory and discuss the effects of numerical parameters. Finally, we use our newly written code to study the dynamics of nonlinear pulse propagation by simulating and studying the propagation of mismatched soliton pulses and Gaussian pulses and, ultimately, the process of SCG. We conclude with chapter 5, in which we present a summary of the results together with conclusions and an outlook.

Chapter 2

Theory of nonlinear pulse propagation

The processes of supercontinuum and Kerr frequency comb generation (SCG and KFCG, respectively) in waveguides are modelled by mathematically describing the nonlinear propagation of a light pulse through a waveguide. To be more precise, we will be investigating the propagation of a complex pulse envelope with some carrier frequency ω_0 , an example of which is shown schematically in figure 2.1. Throughout this report, we assume the envelope to be slowly-varying with respect to ω_0 . A pulse is described as it propagates through some point in space as a function of time, called the fast time. Modelling of pulse propagation typically involves limiting the fast time to a temporal window, large enough to contain the optical pulse, an example of which can be seen in figure 2.1. This window moves with the group velocity at the carrier frequency of the optical pulse through the waveguide. In other words, while the pulse travels with its group velocity down the waveguide, it stays immobile in the centre of the comoving time window (aside from any shape changes the pulse might undergo).

In this chapter, we introduce a set of differential equations that describe nonlinear propagation of light pulses through waveguides. We treat both the nonlinear Schrödinger equation and a generalised variant, which model nonlinear pulse propagation through waveguides. We state these equations and their dimensionless variant if possible, list their underlying assumptions and provide some analytical solutions and results where available.

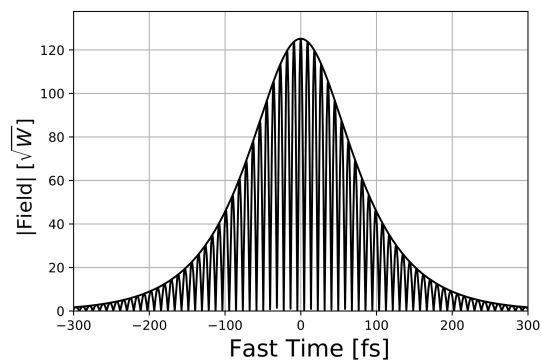


Figure 2.1: Absolute value of a complex pulse envelope with some carrier frequency ω_0 . This pulse satisfies the slowly-varying envelope and phase approximation.

2.1 Nonlinear Schrödinger Equation

The behaviour of electromagnetic (EM) radiation is governed by Maxwell's equations. In the following text, we give a summary of the derivation of the more practical nonlinear Schrödinger equation, including all assumptions made, following the reasoning in [4, chapter 2].

2.1.1 Derivation of the nonlinear Schrödinger equation

Including a polarisation term that represents the material response, Maxwell's equations can be rewritten into the nonlinear, inhomogeneous wave equation for EM waves as

$$\nabla^2 \mathbf{E}(\mathbf{r}, t) - \frac{1}{c^2} \partial_t^2 \mathbf{E}(\mathbf{r}, t) = \mu_0 \partial_t^2 \mathbf{P}(\mathbf{E}; \mathbf{r}, t), \quad (2.1)$$

where c is the speed of light in vacuum, μ_0 the vacuum permeability and \mathbf{E} and \mathbf{P} are the electric field and its induced polarisation field, respectively, both real vector functions, i.e., $\mathbf{E}, \mathbf{P} : \mathbb{R}^3 \times [0, \infty) \rightarrow \mathbb{R}^3$. The polarisation can be written as a function of the electric field as

$$\mathbf{P}(\mathbf{E}; \mathbf{r}, t) = \epsilon_0 (\chi^{(1)} \cdot \mathbf{E} + \chi^{(2)} : \mathbf{E}\mathbf{E} + \chi^{(3)} : \mathbf{E}\mathbf{E}\mathbf{E} + \dots). \quad (2.2)$$

Here, $\chi^{(n)}$ is a time- and position-dependent rank-(n+1) tensor, describing the interaction between all possible combinations of polarisation directions, each at an independent delay. The n dots indicate the convolution of $\chi^{(n)}(\mathbf{r}, t_1, \dots, t_n)$ with $\mathbf{E}(\mathbf{r}, t_1) \dots \mathbf{E}(\mathbf{r}, t_n)$ on the domain $t_i \in (-\infty, 0]$ for all i . Thus, t_i represent the delays of each of the contributing field terms, over which is being integrated.

Since this report is about optical pulses in waveguides made of amorphous materials, we note that amorphous means isotropic and thus the polarisation should obey inversion symmetry, i.e., reversal of the sign of the electric field leads to a reversal of the sign of the polarisation field. For this reason, all the even terms in equation 2.2 must vanish. This makes the third-order the lowest nonlinear order, since the first-order response is linear. For this report, we will be restricting ourselves to third-order nonlinear processes only. This allows us to write the polarisation in terms of its linear and (third-order) nonlinear part, i.e., $\mathbf{P} = \mathbf{P}_L + \mathbf{P}_{NL}$, where

$$\mathbf{P}_L(\mathbf{E}; \mathbf{r}, t) = \epsilon_0 \int_{-\infty}^t \chi^{(1)}(t-s) \cdot \mathbf{E}(\mathbf{r}, s) ds, \quad (2.3a)$$

$$\begin{aligned} \mathbf{P}_{NL}(\mathbf{E}; \mathbf{r}, t) = & \epsilon_0 \int_{-\infty}^{t_1} dt_1 \int_{-\infty}^{t_2} dt_2 \int_{-\infty}^{t_3} dt_3 \\ & \times \chi^{(3)}(t-t_1, t-t_2, t-t_3) : \mathbf{E}(\mathbf{r}, t_1) \mathbf{E}(\mathbf{r}, t_2) \mathbf{E}(\mathbf{r}, t_3). \end{aligned} \quad (2.3b)$$

In this derivation, we will be assuming that light maintains its polarisation along the waveguide. This is not really the case, unless polarisation-maintaining fibers are used, but the approximation works quite well in practice [4, chapter 2]. This will simplify the derivation greatly, since it removes the vectorial nature of the electric field. Furthermore, we assume that pulses are relatively narrowband, i.e., pulses have a spectral width $\Delta\omega$ around some carrier frequency ω_0 such that $\Delta\omega \ll \omega_0$. Note that modulation in the time-domain means adding the sum and difference frequencies in the frequency domain around the carrier frequency. Therefore, pulses can be described by a slowly-varying envelope of maximum frequency $\Delta\omega$, modulated by some carrier frequency ω_0 . This is a valid assumption for pulses as short as 0.1 ps when using light at infrared or shorter wavelengths.

We apply separation of variables to separate the dependence on the propagation direction \hat{z} and time from the two transverse directions \hat{x}, \hat{y} . Using the fact that the polarisation is time-invariant, we define the \hat{x} direction as the polarisation direction. We describe the pulse's dependence on the propagation direction through some slowly-varying, complex envelope $A(z, t)$, modulated with carrier frequency ω_0 . We describe the dependence on the transverse directions through some normalised waveguide mode profile $F(x, y)$. This means that we can write the field as

$$\mathbf{E}(\mathbf{r}, t) = \frac{1}{2} \hat{\mathbf{x}} [F(x, y) A(z, t) \exp(i(\beta_0 z - \omega_0 t)) + c.c.], \quad (2.4)$$

where β_0 is the propagation constant of mode F at frequency ω_0 .

In order to greatly simplify equation 2.2, the nonlinear response is assumed to be instantaneous so that the time dependence of $\chi^{(3)}$ is given by $\delta(t - t_1) \cdot \delta(t - t_2) \cdot \delta(t - t_3)$. This means we will be neglecting the contribution of molecular vibrations, i.e., the Raman effect. The nuclei response is inherently slower than the electronic response. For silica fibers the vibrational (or Raman response) occurs over a time scale of 60–70 fs. The assumption is thus approximately valid for pulse widths >1 ps [4, chapter 2]. For amorphous silicon nitride waveguides for example, Raman scattering can typically be neglected, even for optical pulses with a duration of less than 100 fs [22, 60, 31]. Combining this with equation 2.3b, we get the expression for the nonlinear part of the polarisation field

$$\mathbf{P}_{\text{NL}}(\mathbf{r}, t) = \epsilon_0 \epsilon_{\text{NL}} \mathbf{E}(\mathbf{r}, t), \quad (2.5)$$

where¹

$$\epsilon_{\text{NL}}(\mathbf{r}, t) := \frac{3}{4} \chi_{xxxx}^{(3)} |\mathbf{E}(\mathbf{r}, t)|^2. \quad (2.6)$$

In other words, the effect of the (nonlinear) polarisation can be described by a intensity-dependent refractive index. More precisely, we can write the refractive index as

$$n(I) = n_0 + n_2 \cdot I, \quad (2.7)$$

¹In this report, we will be using "：“ for definition and “=” for equality between defined objects.

where n_0 accounts for the linear part, or first order, and n_2 for the third order of the polarisation. We restrict ourselves to materials with a positive n_2 , which is almost always the case [12]. We normalise the intensity so that $I = |A|^2$ with units W/m^2 . This dependence of the refractive index on the intensity is called the *nonlinear Kerr effect*.

To obtain the pulse propagation equation for $A(z, t)$, it is more convenient to work in the frequency domain. We transform from the time to the frequency domain using the Fourier transform

$$\tilde{A}(z, \omega - \omega_0) := \int_{-\infty}^{\infty} A(z, t) \exp[i(\omega - \omega_0)t] dt, \quad (2.8)$$

so that

$$\tilde{\mathbf{E}}(\mathbf{r}, \omega - \omega_0) = \frac{1}{2} \hat{\mathbf{x}} \left[F(x, y) \tilde{A}(z, \omega - \omega_0) \exp(i\beta_0 z) + c.c. \right]. \quad (2.9)$$

We now transform equation 2.1 to the frequency domain through equation 2.8 and use equations 2.9 and 2.5 for the electric and polarisation fields respectively. We then get the following set of equations that describe the mode field and propagation of the pulse envelope [4, chapter 2]

$$\begin{aligned} \frac{\partial^2 F}{\partial x^2} + \frac{\partial^2 F}{\partial y^2} + \left[\epsilon(\omega) k_0^2 - \tilde{\beta}(\omega)^2 \right] F &= 0, \\ 2i\beta_0 \frac{\partial \tilde{A}}{\partial z} + \left(\tilde{\beta}^2(\omega) - \beta_0^2 \right) \tilde{A} &= 0. \end{aligned} \quad (2.10)$$

Here, $\partial^2 \tilde{A} / \partial z^2$ was neglected since \tilde{A} is assumed to be a slowly-varying function of z . Additionally, $\tilde{\beta}$ is the propagation constant of the mode $F(x, y)$. Furthermore, we express $\tilde{\beta}$ in terms of the propagation constant β as calculated when ignoring nonlinear effects plus a term $\delta\beta$ that corrects for the Kerr effect.

$$\begin{aligned} \tilde{\beta}(\omega) &:= \beta(\omega) + \delta\beta(\omega), \\ \delta\beta(\omega) &= \frac{\omega^2 n_0(\omega)}{c^2 \beta(\omega)} \frac{\iint_{\mathbb{R}^2} n_2(x, y, \omega) \cdot I \cdot |F(x, y)|^2 dx dy}{\iint_{\mathbb{R}^2} |F(x, y)|^2 dx dy}. \end{aligned} \quad (2.11)$$

Here, in good approximation, the modal distribution F is taken to be unaffected by the Kerr effect. Now we expand both β and $\delta\beta$ around ω_0 using a Taylor expansion, denoting the coefficients as

$$\beta_k := \partial^k \beta(\omega) / \partial \omega^k |_{\omega=\omega_0}. \quad (2.12)$$

By this definition, we have that β_1 is the inverse of the group velocity v_g and β_2 is the group velocity dispersion (GVD).

For simplicity we truncate β after the second-order term and use $\delta\beta \approx \delta\beta_0$ by the narrowband assumption $\delta\omega \ll \omega_0$. At a later state we will include higher-order

terms to increase the spectral bandwidth of the model. We can now write equation 2.10 in the time domain as

$$\frac{\partial A}{\partial z} + \beta_1 \frac{\partial A}{\partial t} + \frac{i\beta_2}{2} \frac{\partial^2 A}{\partial t^2} = i\delta\beta_0 A = i\gamma|A|^2 A, \quad (2.13)$$

where the nonlinear parameter γ is defined as

$$\gamma := \frac{\omega_0 n_2 \iint_{\mathbb{R}^2} |F(x, y)|^4 dx dy}{c \iint_{\mathbb{R}^2} |F(x, y)|^2 dx dy} = \frac{\omega_0 n_2}{c A_{\text{eff}}}. \quad (2.14)$$

Here, the assumptions were made that the spatial dependence of n_2 and frequency-dependence of the mode are negligible in order to simplify our calculations. Furthermore, A_{eff} denotes the effective mode area of the waveguide mode F , defined by

$$A_{\text{eff}}(F) := \frac{(\iint_{\mathbb{R}^2} |F(x, y)|^2 dx dy)^2}{\iint_{\mathbb{R}^2} |F(x, y)|^4 dx dy}. \quad (2.15)$$

The effective mode area is a measure for the transverse size of a mode. This can be illustrated by taking the indicator function $\mathbf{1}_A$ over some area $A \subset \mathbb{R}^2$ as the mode. One readily checks that $A_{\text{eff}}(\mathbf{1}_A) = (|A|)^2/|A| = |A|$, i.e., the effective mode area equals the size of A .

If we now switch to a comoving temporal frame of reference that propagates with the group velocity $v_g = \beta_1^{-1}$ by defining $T := t - z/v_g$, we get the *nonlinear Schrödinger equation* (NLSE)

$$i \partial_z A(z, T) - \frac{\beta_2}{2} \partial_T^2 A + \gamma |A|^2 A = 0. \quad (2.16)$$

Equation 2.16 is the most simple equation describing nonlinear pulse propagation. It includes the most important features, namely GVD and the Kerr effect, and allows us to get some analytical results. However, we will later relax the narrowband approximation in order to model supercontinuum generation more accurately. One important property of the NLSE is that it preserves pulse energy, as it can be proven that [48]

$$\int_{\mathbb{R}} |A(z, T)|^2 dT = \int_{\mathbb{R}} |A(0, T)|^2 dT \quad \text{for all } z > 0. \quad (2.17)$$

2.1.2 Dimensionless form

When performing a numerical or analytical analysis of an equation, it is usually beneficial to transform the equation in question into a dimensionless or normalised form. This removes any concerns about the units of any numerical value and allows for scaling of variables, which can be used to prevent overflow errors when using numerical methods. Additionally, it can simplify the equation by minimising

the number of parameters. This means that a set of dimensionless parameters represents a whole class of systems. Every combination of parameters that lead to the same dimensionless parameters, leads to the same solution. In case of the NLSE, equation 2.16 depends on two parameters, namely the GVD β_2 and the nonlinear parameter γ . However, the NLSE can be rewritten in a dimensionless form depending on only one boolean parameter $\text{sgn}(\beta_2)$, namely [4, chapter 5]

$$i \partial_\xi u(\xi, \tau) - \frac{1}{2} \text{sgn}(\beta_2) \partial_\tau^2 u + |u|^2 u = 0, \quad (2.18)$$

by introducing three dimensionless or normalised quantities

$$u := \frac{AN}{\sqrt{P_0}}, \quad \xi := \frac{z}{L_D}, \quad \tau := \frac{T}{T_0}. \quad (2.19)$$

Here, P_0 is the pulse peak power and T_0 the pulse width of the incident pulse. Note that T_0 is not well-defined in general. In the case of a hyperbolic secant or Gaussian pulse shape, it is defined as the scaling factor, i.e., through $\text{sech}(T/T_0)$ or $\exp[-(T/T_0)^2]$ respectively. This defines T_0 in our case, since these are the only two pulse shapes we will be considering in this report. Note that for the hyperbolic secant shape, this leads to a corresponding full-width half-max width of $T_{\text{FWHM}} \approx 1.76 T_0$. Continuing, the dispersion length $L_D = T_0^2/|\beta_2|$ and the nonlinear interaction length $L_{\text{NL}} = 1/\gamma P_0$ are characteristic length scales over which the dispersive and nonlinear effects affect the pulse respectively. The parameter N , defined by

$$N^2 := L_D/L_{\text{NL}}, \quad (2.20)$$

is determined by the system parameters $\gamma, |\beta_2|$ and the incident pulse parameters T_0, P_0 and is a measure for the relative strength of the GVD and Kerr effects. Furthermore, it determines the stable solution of the system, as will become clear in the next subsection.

2.1.3 Self-phase modulation & soliton solutions

The Kerr effect modifies the phase of a pulse. This can be analysed by solving equation 2.18 without GVD ($\beta_2 = 0$), using a plane-wave

$$u(\xi, \tau) = u_0(\tau) \exp[i \cdot \varphi_{\text{NL}}(\xi, \tau)], \quad (2.21)$$

where $u_0(\tau) := u(0, \tau)$. Equation 2.21 is a solution of equation 2.18 if and only if

$$\varphi_{\text{NL}}(\xi, \tau) = -\xi \cdot |u_0(\tau)|^2, \quad (2.22)$$

which is the nonlinear phase change due to the Kerr effect. Here we have used $\varphi_{\text{NL}}(\xi, \tau) = 0$ if $u_0 = 0$. From this we can now get the change in the instantaneous frequency in a pulse

$$\delta\omega_{\text{NL}}(\xi, \tau) = -\frac{\partial\varphi_{\text{NL}}(\xi, \tau)}{\partial\tau} = \xi \cdot \frac{\partial|u_0(\tau)|^2}{\partial\tau}. \quad (2.23)$$

In other words, the frequency shift in a pulse due to the Kerr effect depends on the slope of its intensity and increases linearly with propagation distance ξ . This is illustrated in figure 2.2, which schematically shows the instantaneous frequency after a certain propagation distance as a function of time within the optical pulse. This effect, in which a pulse alters its own phase and frequency by altering the refractive index locally through the Kerr effect, is called self-phase modulation (SPM). So, when a pulse travels through a medium with a positive n_2 , it will introduce a redshift in the front of the pulse and a blueshift in the back of the pulse. In other words, it creates a chirp in the pulse. A chirp is a variation of the instantaneous frequency inside a pulse. Note that n_2 is positive for the waveguides we are considering in this report.

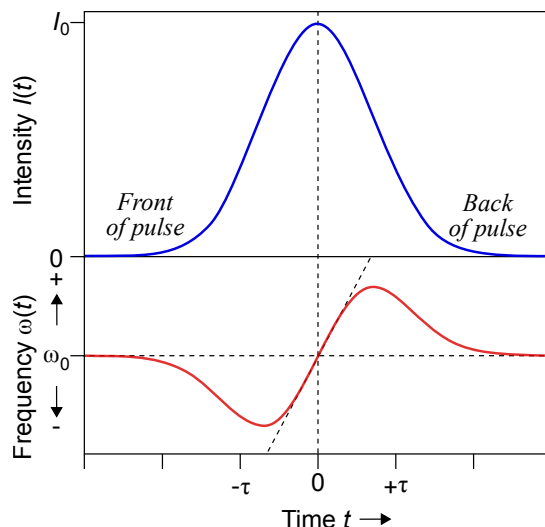


Figure 2.2: Effect of self-phase modulation, where the front of a pulse undergoes a redshift and the back a blueshift due to the nonlinear Kerr effect.

Normally, higher frequencies travel with a lower group velocity than lower frequencies. This is called normal GVD and it leads to a chirp similar to that of SPM. Now, if higher frequencies happen to travel with a higher group velocity than lower frequencies, i.e., anomalous GVD or $\beta_2 < 0$, the GVD will create a chirp in the pulse that is opposite to the SPM. The SPM combined with anomalous GVD leads to sharpening of the pulse. This self-sharpening of a pulse is called modulation instability and it will continue until the pulse reaches a steady-state. A pulse for which the dispersive and nonlinear effects cancel each other out is called a soliton, which, theoretically, will travel indefinitely without changing its shape.

Mathematically, the shape of such a soliton can be obtained by solving equation 2.18 using the inverse scattering method [50]. This yields a sequence of solutions. To which of these solutions the system will converge depends solely on N . If $N = 1$, the initial conditions correspond to the first-order or fundamental soliton solution. This fundamental soliton looks as follows in the normalised and nonnormalised

case, respectively,

$$u_{\text{sol}}^{(1)}(\xi, \tau) = \text{sech}(\tau) \exp(i\xi/2), \quad (2.24a)$$

$$A_{\text{sol}}^{(1)}(z, T) = \sqrt{P_0} \text{sech}(T/T_0) \exp(iz/2L_D). \quad (2.24b)$$

We observe that the fundamental soliton depends on both the peak power P_0 and the pulse width T_0 , as well as on the GVD β_2 and the nonlinear parameter γ , which are material properties. Now, P_0 and T_0 are linked through equation 2.20, meaning that, given a waveguide, there is only one degree of freedom for the fundamental soliton.

For $N = 2$ we get a so-called second-order soliton, which is given by [49]

$$u_{\text{sol}}^{(2)}(\xi, \tau) = \frac{4 [\cosh(3\tau) + 3 \exp(4i\xi) \cosh(\tau)]}{\cosh(4\tau) + 4 \cosh(2\tau) + 3 \cos(4\xi)}. \quad (2.25)$$

Note that $u_{\text{sol}}^{(2)}(0, \tau) = 2 u_{\text{sol}}^{(1)}(0, \tau)$. Furthermore, the absolute value of $u_{\text{sol}}^{(2)}$, which is proportional to the square root of the intensity I , is a periodic function in ξ with period $\xi_0 = \pi/2$. Similarly, soliton solutions exist for all $N \in \mathbb{N}^1$. While the analytical solutions are less straight-forward to write down for higher-order solitons, the initial conditions are, for all N , given by

$$u_{\text{sol}}^{(N)}(0, \tau) = N \text{sech}(\tau). \quad (2.26)$$

In addition, the soliton period ξ_0 remains $\pi/2$ for the intensity for all $N \in \mathbb{N}^1$ [4].

Let us suppose now that we somehow have introduced a hyperbolic secant shaped pulse, as given by equation 2.26, into our waveguide, but with a non-integer value for N , let's call this $\tilde{N} \in \mathbb{R} \setminus \mathbb{N}^1$. The pulse shape then transforms itself into the soliton with nearest order N , i.e., projection of \tilde{N} onto \mathbb{N}^1 , through modulation instability [4]. Furthermore, many pulse types are transformed into soliton shapes under the influence of the Kerr effect and anomalous GVD, most notably Gauss-shaped pulses. In this process, part of the pulse energy is radiated away in the form of continuum radiation, which decays with $\xi^{-1/2}$ [4].

In addition to the normal (bright) soliton, there also exist dark soliton solutions to the NLSE. Where a bright soliton can be described as a pulse of heightened intensity on a low- or zero-intensity background, a dark soliton consists of a dip in the intensity on an otherwise constant background. Dark solitons are possible in case of normal GVD, i.e., $\beta_2 > 0$. The general form is given by

$$u_{\text{dark}}(\xi, \tau) = \eta \left[B \tanh(\zeta) - i\sqrt{1 - B^2} \right] \exp(i\eta^2 \xi), \quad (2.27)$$

$$\zeta := \eta B (\tau - \tau_s - \eta B \sqrt{1 - B^2}),$$

where the so-called blackness parameter B governs the depth of the dip ($|B| \leq 1$). For $|B| = 1$, the dip falls to zero. Furthermore, η is the background amplitude and τ_s the dip location. Figure 2.3 shows a number of dark solitons with different values for B [41, 4]. Note that although the dark soliton with a constant background

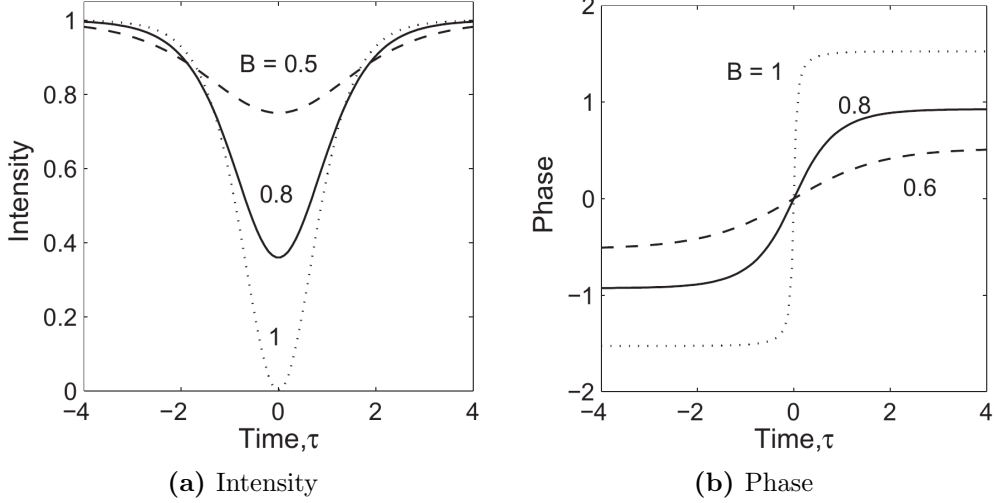


Figure 2.3: Intensity (a) and phase (b) profiles of dark solitons for several values of the blackness parameter B , ranging from 0.5 to 1 [4].

that stretches out indefinitely, as defined here, is a mathematical solution to the NLSE, it is not a physical solution, since it holds infinite energy. Dark solitons are still relevant solutions, since they have been realised experimentally on a finite, constant background [20].

2.2 Generalised Nonlinear Schrödinger Equation

As this report is about spectral broadening of pulses, a second-order expansion of $\beta(\omega)$ will not be sufficient and the inclusion of higher-order terms in the expansion of $\beta(\omega)$ is required to model dispersion accurately over a larger bandwidth. Together with the inclusion of other nonlinear processes as self-steepening or optical shock-wave formation, and nonlinear Raman scattering, this changes the NLSE into the so-called *generalised nonlinear Schrödinger equation* (GNLSE)² [18]

$$\begin{aligned} \partial_z A(z, T) = & -\frac{1}{2}\alpha A + i \sum_{k=2}^{\infty} \left[\frac{i^k}{k!} \beta_k \partial_T^k \right] A + i\gamma \left(1 + \frac{i}{\omega_0} \partial_T \right) \\ & \times \left[(1 - f_R) A |A|^2 + f_R A \int_0^{\infty} h_R(T') |A(z, T - T')|^2 dT' + i\Gamma_R(z, T) \right]. \end{aligned} \quad (2.28)$$

The first term on the right-hand-side (RHS) describes absorption, where α is the (power) absorption coefficient. The second term describes dispersion in the form of a Taylor expansion of β around the frequency ω_0 . The rest of the terms describe the nonlinear effects. The three terms within the square brackets describe the Kerr effect, Raman scattering and Raman noise, respectively, while the term before the square brackets describes self-steepening. The Raman noise is represented by the

²The \times -symbol here is used to denote application of an operator, not multiplication.

stochastic variable Γ_R and it models spontaneous Raman fluctuations. Raman scattering is turned off in equation 2.28 by setting $f_R = 0$, while self-steepening is turned off by assuming $\|\partial_T/\omega_0\| \ll 1$.

Equation 2.28 has been used extensively to model nonlinear pulse propagation [18]. Note that setting $\alpha = 0, \beta_k = 0$ for $k > 2, f_R = 0, \Gamma_R = 0$ and ignoring the derivative w.r.t. T in the self-steepening term yields the NLSE as seen in equation 2.16.

In the following section, we will be stating some semi-analytical results obtained from the GNLSE. These results will be used in chapter 4 to validate simulation results.

2.2.1 Fundamental soliton and third-order dispersion

As discussed in section 2.1.3, the NLSE admits a set of stable solutions called solitons. The first of these is the fundamental soliton, which, according to the NLSE, travels indefinitely without changing its shape. However, when using the GNLSE, the presence of higher-order dispersion or nonlinear processes other than the Kerr effect distorts the exact balance between GVD and self-phase modulation that leads to the formation of solitons. Here we consider the effect of third-order dispersion (TOD) on the propagation of a fundamental soliton, i.e., we consider equation 2.28 with only third-order dispersion included, so that we get

$$i \partial_z A(z, T) - \frac{\beta_2}{2} \partial_T^2 A + \gamma |A|^2 A = \frac{i\beta_3}{6} \partial_T^3 A. \quad (2.29)$$

Under the assumption that β_3 is sufficiently small so that the soliton approximately maintains its shape, the moment method can be used to solve equation 2.29 [4, chapter 4]. In the moment method, the pulse is assumed to maintain a specific shape and only the parameters of said shape are affected during propagation. For a soliton pulse, these parameters are its chirp, amplitude, phase, width and center T_s w.r.t. the comoving frame. It can be shown that the effect of TOD is to make the soliton peak drift through the time window as it propagates, i.e., altering the group velocity of the soliton. A soliton pulse with a variable center can be written down as

$$A(z, T) = \operatorname{sech}\left(\frac{T - T_s(z)}{T_0}\right) \exp(iz/2L_D), \quad (2.30)$$

with T_s the temporal center. The drift $T_s(z)$ is then given by [4]

$$T_s(z) = (\beta_3/6T_0^2) z, \quad (2.31)$$

meaning that the group velocity of the soliton is altered by

$$\Delta v_g = -6T_0^2/\beta_3. \quad (2.32)$$

This shows that a fundamental soliton is a stable solution that alters its parameters due to perturbations, but otherwise continues to propagate undisturbed.

2.2.2 Soliton fission

In addition to the fundamental soliton, the NLSE permits a soliton solution of order N for every $N \in \mathbb{N}^1$. Such a solution with order $N > 1$ is a superposition of N fundamental solitons moving together at the same group velocity. When $N > 1$, the temporal profile of the higher-order soliton is no longer constant upon propagation. Interference between the N weakly bound fundamental solitons leads to oscillation of the higher-order soliton, as discussed in section 2.1.3.

However, as this higher-order soliton is a weakly-bounded state, any effect that is added to the NLSE that affects the group velocity in a frequency-dependent manner, such as TOD, will cause a higher-order soliton to break-up into its N components. Every component is then a fundamental soliton that will continue to propagate at its own group velocity. These solitons are characterised by their width and peak power. For the k th component, these are related to those of the original higher-order soliton through [42, 4]

$$T_k = \frac{T_0}{2N + 1 - 2k}, \quad P_k = \frac{P_0}{N^2} (2N + 1 - 2k)^2, \quad k \in 1, \dots, N. \quad (2.33)$$

This break-up process of a higher-order soliton is called soliton fission. Note that the total energy in the resulting fundamental solitons is always lower than that of the original higher-order soliton. During soliton fission, part of the energy is shed in the form of a so-called dispersive wave (see next section).

2.2.3 Dispersive waves

Dispersive waves are linear waves emitted from pulses during processes such as soliton fission and modulation instability. Efficient energy transfer from a pulse to a dispersive wave with a specific wave number is possible when the dispersive wave is phase matched to the pulse. The emission of dispersive waves is a process that is formally equivalent to Cherenkov radiation [5]. Classical Cherenkov radiation appears when a small object (particle) moves in a medium with a velocity exceeding the phase velocity of the waves in the given medium. In this section, we present two methods for determining for what frequencies a linear wave is phase-matched to a soliton, i.e., at what frequency we can expect dispersive waves to emerge.

For phase-matching, the wavenumber of the soliton must equal the wavenumber of a linear wave. The wave number of a soliton β_{sol} with a carrier frequency ω_0 is [5, 37]

$$\begin{aligned} \beta_{\text{sol}}(\omega_0) &= \beta_0 + \omega_0 \beta_1 + \frac{1}{2} \gamma P_0, \\ &= \beta_0 + \omega_0 \beta_1 + \Delta \beta_{\text{sol}}(\omega_0), \end{aligned} \quad (2.34)$$

where $\Delta \beta_{\text{sol}}$ is the wavenumber of the envelope in a comoving frame. Note that since we are not considering absorption in this section, the wavenumber and propagation

constant β can be used interchangeably. The dispersive wave is a linear wave with an envelope of shape $\exp[i(k_{\text{lin}}z - \Delta\omega t)]$, where $\Delta\omega := \omega - \omega_0$. Inserting the linear wave in the NLSE, as shown in equation 2.16, gives us the following dispersion relation

$$\begin{aligned}\beta_{\text{lin}}(\omega) &= \beta_0 + \omega_0\beta_1 + \frac{\beta_2}{2} \Delta\omega^2, \\ &= \beta_0 + \omega_0\beta_1 + \Delta\beta_{\text{lin}}(\Delta\omega).\end{aligned}\tag{2.35}$$

Here, the contribution of the nonlinear term in the NLSE to the wave number was neglected. Note that both the soliton and the linear wave are envelopes over the same carrier wave at frequency ω_0 . This means that the two are phase-matched if and only if $\Delta\beta_{\text{sol}}(\omega_0) = \Delta\beta_{\text{lin}}(\omega_D)$, where ω_D is the frequency for which we have phase-matching.

Since a soliton requires anomalous GVD, β_2 must be negative. Thus, $\Delta\beta_{\text{lin}} < 0$ while $\Delta\beta_{\text{sol}} > 0$. This means no phase-matching is possible, no energy is radiated from the soliton and the soliton is stable. However, when considering TOD as in equation 2.29, the linear wave obeys the dispersion relation

$$\Delta\beta_{\text{lin}}(\omega) = \frac{\beta_2}{2} \Delta\omega^2 + \frac{\beta_3}{6} \Delta\omega^3.\tag{2.36}$$

This means there is a phase-matched linear wave at frequency [5]

$$\omega_D = \omega_0 + 6/\beta_3 \left[1/2 + (\beta_3^2 P_0)/18 + O(\beta_3\sqrt{P_0})^4 \right],\tag{2.37}$$

i.e., TOD causes dispersive waves to be radiated from a fundamental soliton. Any process that affects the dispersion relation of waves may result in energy being transferred from a soliton to linear dispersive waves. In general, the dispersion relation can be obtained from the GNLSE, as shown in equation 2.28. Again neglecting contributions from nonlinear processes, we get the following dispersion relation

$$\Delta\beta_{\text{lin}}(\omega) = \sum_{k=2}^{\infty} \frac{\Delta\omega^k}{k!} \beta_k.\tag{2.38}$$

Directly equating the wavenumber of a soliton to that of a linear wave is another approach to determine frequencies for which the two are phase-matched. the phase-matching condition between a dispersive wave at a frequency ω_D and a dispersionless soliton is [37, 29, 4]

$$\beta(\omega_D) = \beta(\omega_0) + (\omega_D - \omega_0)\beta_1 + \frac{1}{2}\gamma P_0.\tag{2.39}$$

If we now neglect the nonlinear contribution to the soliton wavenumber and expand the wavenumber β around ω_0 in a Taylor expansion, we get the following phase-matching condition

$$\beta(\omega_D) - \beta(\omega_0) - (\omega_D - \omega_0)\beta_1 = \beta_{\text{int}}(\omega_D) = 0,\tag{2.40}$$

where

$$\beta_{\text{int}}(\omega_D) := \sum_{k=2}^{\infty} \frac{(\omega_D - \omega_0)^k}{k!} \beta_k. \quad (2.41)$$

Here, the part of the Taylor expansion including all terms starting from the second-order is called the integrated dispersion β_{int} . The integrated dispersion only depends on the dispersion relation $\beta(\omega)$ and the carrier frequency ω_0 . Once this information is obtained, the frequencies for dispersive waves can be found by finding the roots of the integrated dispersion [29].

Chapter 3

Numerical methods

In the previous chapter, we introduced the equations that describe the nonlinear propagation of pulses through waveguides, namely the NLSE (equation 2.18) and the GNLSE (equation 2.28). We considered some analytical solutions and some approximate, theoretical properties. However, in most cases, these nonlinear PDEs do not permit exact or even approximate analytical solutions, implying that a numerical approach is necessary to study nonlinear optical effects in waveguides. Most available numerical methods can be divided into two categories, namely, finite-difference methods and pseudo-spectral methods. Of the finite-difference methods, the Crank-Nicholson implicit [14] and Hopscotch [27] methods are two well-known examples. Of the pseudo-spectral methods, the split-step Fourier method is the most common example. In this report we will be focusing on two pseudo-spectral methods, the first of which is the symmetric split-step Fourier method (SSFM) [23], a classic method that is the most commonly used for these types of problems. SSFM is a more computationally efficient method than most finite-difference methods [4, 55]. The second method is the 4th-order Runge-Kutta method [13] in the interaction picture (RK4IP), a relatively new method, promising a higher order of accuracy and increased computational efficiency when compared to SSFM [36]. What makes these methods pseudo-spectral, is that they solve part of the problem in the frequency domain by using the fast Fourier transform (FFT). Both methods were implemented using Python, using standard best practices in scientific computing [57]. The calculations, most notably the FFTs, were done using the numerical computing library NumPy/SciPy [1].

In this chapter, in section 3.1, we start by introducing the notation of the relevant PDEs, i.e., the NLSE and the GNLSE, in terms of generalised operators. This will allow us to introduce the methods in a more convenient and general way. Next, in sections 3.2 and 3.3, we introduce the numerical schemes by which SSFM and RK4IP are defined, respectively. In addition, we consider some of their numerical properties. Finally, in section 3.4, we introduce the tools we use for analysing the quality of our numerical solutions and investigate the convergence of these solutions.

3.1 Notation

In this section, we introduce the notation that will allow us to describe the methods in a convenient and general manner in the following sections. All methods used rely on writing the PDE in the general form

$$\partial_z A(z, T) = \{D(T) + N(A(z, T))\} A(z, T). \quad (3.1)$$

Here, D and N are the linear and nonlinear operators that represent the PDE, respectively. Note that we call the independent variables z, T , similar to the case of the GNLSE. Thus, in our setting, $A(z, T)$ represents the field envelope $A(z, T)$ as a function of the propagation distance z and time T in case the PDE equals the GNLSE, while $A(z, T)$ represents the normalised envelope $u(\xi, \tau)$ as a function of normalised propagation distance ξ and time τ in case of the dimensionless NLSE, as defined in section 2.1.2.

Consider the dimensionless NLSE, as seen in equation 2.18. Using $A(z, T) = u(\xi, \tau)$, we then get the following operators

$$D(\tau) = -\frac{i}{2} \text{sgn}(\beta_2) \partial_\tau^2, \quad N(A) = i |A|^2. \quad (3.2)$$

Now, what makes the methods treated in this chapter pseudo-spectral, is that the linear operator D is treated in the frequency domain. This is done by transforming $D(\tau) A(\xi, \tau)$ to the frequency domain, around carrier frequency ω_0 , to get $\tilde{D}(\omega - \omega_0) A(\xi, \omega - \omega_0)$ by using the transformation from equation 2.8. To deal with the time derivative in D , we use the property of the Fourier transform

$$\begin{aligned} \mathcal{F}\{\partial_t f(t)\}(\omega - \omega_0) &= \int_{-\infty}^{\infty} \partial_t f(t) \cdot \exp(i(\omega - \omega_0)t) dt \\ &= - \int_{-\infty}^{\infty} f(t) \cdot \partial_t \exp(i(\omega - \omega_0)t) dt \\ &= \mathcal{F}\{\partial_t f(t)\}(\omega - \omega_0) = -i(\omega - \omega_0) \cdot \hat{f}(\omega - \omega_0). \end{aligned} \quad (3.3)$$

Here, we used integration by parts, requiring that

$$\left[f(t) \cdot \exp(i(\omega - \omega_0)t) \right]_{t \rightarrow -\infty}^{t \rightarrow \infty} = 0. \quad (3.4)$$

This holds if we assume $f(T)$ vanishes as $T \rightarrow \pm\infty$. This is true if the field f is continuous and holds finite energy, which is the case for all light pulses considered in this report.

Applying equation 3.3, we get for the D -operator as seen in equation 3.2

$$\begin{aligned} \tilde{D}(\omega - \omega_0) \tilde{A}(\xi, \omega - \omega_0) &= \int_{-\infty}^{\infty} D(\tau) A(\xi, \tau) \cdot \exp(i(\omega - \omega_0)\tau) d\tau, \\ &= \frac{i}{2} \text{sgn}(\beta_2) (-(\omega - \omega_0))^2 \cdot \tilde{A}(\xi, \omega - \omega_0), \\ \implies \tilde{D}(\omega - \omega_0) &= \frac{i}{2} \text{sgn}(\beta_2) (\omega - \omega_0)^2. \end{aligned} \quad (3.5)$$

By performing this transformation, the difficulty of discretising the derivatives w.r.t. τ is effectively replaced by the difficulty of performing a Fourier transform. Performing a Fourier transform can be done efficiently by using the fast Fourier transform and inverse fast Fourier transform (both denoted FFT) [17]. It is the efficiency of this FFT algorithm that makes SSFM faster than most finite-difference-based methods [4, 55]. The use of FFT deals with the finite time window by imposing periodic boundary conditions on A . For most cases, where the pulse envelope vanishes as $T \rightarrow \pm\infty$, this means that the time window needs to be wide enough, so that A is negligible at both edges of the window.

Similarly, for the GNLSE, as in equation 2.28, we get the following operators that describe the field envelope $A(z, T)$

$$\begin{aligned}
D(T) &= -\frac{1}{2}\alpha + i \sum_{k=2}^{\infty} \left[\frac{i^k}{k!} \beta_k \partial_T^k \right], \\
\implies \tilde{D}(\omega - \omega_0) &= -\frac{1}{2}\alpha \cdot \delta(\omega - \omega_0) + i \sum_{k=2}^{\infty} \left[\frac{\beta_k}{k!} \cdot (\omega - \omega_0)^k \right], \\
N(A) &= \frac{i\gamma}{A} \left(1 + \frac{i}{\omega_0} \partial_T \right) \\
&\quad \times \left\{ (1 - f_R) A |A|^2 + f_R A \int_0^{\infty} h_R(T') |A(z, T - T')|^2 dT' + i \Gamma_R \right\}.
\end{aligned} \tag{3.6}$$

Here we used the identity from equation 3.3 and the transform of the identity function $\mathcal{F}\{\mathbf{1}\}(\omega - \omega_0) = \delta(\omega - \omega_0)$. For the GNLSE especially, it becomes clear why one would want to treat the linear operator in the frequency domain. Accurately approximating theoretically infinite derivatives in a computationally efficient manner is quite the challenge when taking a finite-difference approach, while it does not influence the difficulty of using FFT.

This concludes the generalisation of the NLSE and the GNLSE to the form as in equation 3.1. We will now proceed to describe the numerical methods used in this report, using this formalism.

3.2 Split-Step Methods

Once the PDE has been written in the form 3.1, a number of methods can be applied to solve it. One family of methods consists of the split-step methods [35], which treat equation 3.1 as an ODE, where instead of a scalar function of z , we have a mapping from z to an (integrable) function of T , i.e., $[A(z)](T)$ or $A : [0, \infty) \rightarrow L^2(\Omega)$, with $\Omega \subseteq \mathbb{R}$ the time window.¹ This idea is encompassed

¹ $L^2(\Omega)$ is the function space consisting of all functions $f : \Omega \rightarrow \mathbb{C}$ for which $\|f\|_2$ is bounded, see equation 3.25.

by the notion of a flow operator. A flow operator is a mapping from the initial condition onto the solution of a differential equation as a function of the independent variable, in our case z . The notation is as follows

$$A(z, T) = \varphi^{(z)}(A(0, T)), \quad (3.7)$$

where $\varphi^{(z)}$ is the flow operator, sometimes denoted as $\exp(zD)$. Note that $\varphi^{(0)}$ is the identity function and that the identity $\varphi^{(z_1)} \circ \varphi^{(z_2)} = \varphi^{(z_1+z_2)}$ holds. If we now split equation 3.1 into two differential equations, one for the linear part and one for the nonlinear part, we can define two flow operators, one for each. For the linear part

$$\partial_z v(z, T) = D(T) v(z, T), \quad (3.8)$$

where v is some solution to this linear PDE, we have the flow operator $\varphi_D^{(z)}$. Here, $\varphi_D^{(z)}$ can be understood as the semigroup, generated by the unbounded operator D . An expression for $\varphi_D^{(z)}$ can be obtained in the frequency domain using a Fourier transform, namely [8, 46]

$$\tilde{v}(z, \omega - \omega_0) = \tilde{\varphi}_D^{(z)}(\tilde{v}(0, \omega - \omega_0)) = \exp\left(z\tilde{D}(\omega - \omega_0)\right) \cdot \tilde{v}(0, \omega - \omega_0), \quad (3.9)$$

For the nonlinear part

$$\partial_z w(z, T) = N(w) w(z, T), \quad (3.10)$$

where w is some solution to this nonlinear PDE, we get the flow operator $\varphi_{\text{NL}}^{(z)}$, which is given by

$$w(z, T) = \varphi_{\text{NL}}^{(z)}(w(0, T)) = \exp\left(\int_0^z N(w(z')) dz'\right) w(0, T). \quad (3.11)$$

Similarly, we can write down the solution to equation 3.1 as a flow operator $\varphi_{\text{NLSE}}^{(z)}$, namely

$$A(z, T) = \varphi_{\text{NLSE}}^{(z)}(A(0, T)). \quad (3.12)$$

Up until here, all results have been exact. The split-step method applies operator splitting to $\varphi_{\text{NLSE}}^{(z)}$ to separate the linear from the nonlinear part. Two classical methods for operator splitting are the Lie formula, which looks like $\varphi_L^{(z)} := \varphi_D^{(z)} \circ \varphi_{\text{NL}}^{(z)}$, and the Strang formula, which looks like $\varphi_S^{(z)} := \varphi_D^{(z/2)} \circ \varphi_{\text{NL}}^{(z)} \circ \varphi_D^{(z/2)}$ [9, 53]. The approximate flux operator is then applied over a small propagation step h . The integral over N in equation 3.11 is approximated over this small step by

$$\int_z^{z+h} N(A(z')) dz' \approx h N(A(z)).$$

In the case of Lie operator splitting, we get the simple split-step method

$$A(z+h, T) = \varphi_L^{(h)}(A(z, T)) = \exp(hD) \exp(hN(A(z, T))) A(z, T). \quad (3.13)$$

In the case of Strang operator splitting we get the symmetric split-step method

$$\begin{aligned} A(z+h, T) &= \varphi_S^{(h)}(A(z, T)) \\ &= \exp(h/2D) \exp(hN(A(z, T))) \exp(h/2D) A(z, T). \end{aligned} \quad (3.14)$$

Here, the $\exp(h/2D)$ -operator is evaluated in the Fourier domain using FFTs, so we deal with the possibly large numbers of higher-order derivatives in an elegant manner. We note that the operator exponential $\exp(h/2\tilde{D})$ is defined by equation 3.9 and either equation 3.2 or 3.6. We can now write

$$A(z+h, T) = \mathcal{F}^{-1} \circ \tilde{\varphi}_D^{(h/2)} \circ \mathcal{F} \circ \varphi_{NL}^{(h)} \circ \mathcal{F}^{-1} \circ \tilde{\varphi}_D^{(h/2)} \circ \mathcal{F}\{A(z, T)\}, \quad (3.15)$$

where $\Delta\omega := \omega - \omega_0$ and $\tilde{\varphi}_D^{(h/2)} = \exp(h/2\tilde{D}(\Delta\omega))$. This method is finally called the *symmetric split-step Fourier method* (SSFM). For SSFM, four FFTs per propagation step are required: two to transform the $\exp(h/2D)$ -operators to the frequency domain and two to transform them back again, to allow for the $\exp(hN)$ -operator to be dealt with in the time domain. Note that, both \tilde{D} and N are operators that simply multiply their input by some factor. Furthermore, since $\exp(h/2\tilde{D})$ does not depend on the solution A , it can be calculated beforehand. Also note that every step starts with a forward FFT and ends with a backward FFT. If intermediate results in the time domain are not required, the method in equation 3.15 can be made more efficient without affecting its properties by writing it down as [4]

$$A(z_{\max}, T) = \mathcal{F}^{-1} \circ \prod_{i=1}^N \left(\mathcal{F} \circ \varphi_{NL}^{(h)} \circ \mathcal{F}^{-1} \circ \tilde{\varphi}_D^{(h)} \right) \circ \mathcal{F}\{A(0, T)\}, \quad (3.16)$$

where N is the number of propagation steps that are taken to integrate over $(0, z_{\max}]$ and the multiplication sign "∏" is meant to signify application, rather than multiplication. Note that, in addition to reducing the amount of FFTs required per step from four to two, the two instances of the linear operator $\tilde{\varphi}_D^{(h/2)}$ have been combined in $\tilde{\varphi}_D^{(h)}$. This can be done, since $\tilde{\varphi}_D^{(h)}$ does not depend on z . This method is called the *reduced split-step Fourier method* [4, 35].

The fact that the operators D and N generally do not commute, means that the splitting of the operators, using either Lie or Strang operator splitting, gives rise to an error. The Baker-Hausdorff formula² [56]

$$\exp(x) \exp(y) = \exp \left(x + y + \frac{1}{2}[x, y] + \frac{1}{12}[x - y, [x, y]] + O(x^2) \cdot O(y^2) \right), \quad (3.17)$$

can be used to obtain the order of convergence of this error, by choosing $x = hD$, $y = hN$. This way, it can be shown that this error is locally 2nd-order in h for the Lie formula and 3rd-order for the Strang formula. Thus, the simple split-step Fourier method is a globally 1st-order method in h and SSFM a globally 2nd-order method [35].

In this report, SSFM is one of the methods that we are investigating. However, through the years, many variations on the split-step method have been created for more efficient simulation of supercontinuum generation. One popular scheme is the one introduced by Blow and Wood, which in turn has been implemented in many different variations [11, 36].

²The brackets $[x, y] := xy - yx$ denote commutation.

3.3 RK4IP Method

A fundamentally different method is the fourth-order Runge-Kutta method (RK4), which can be directly used to integrate equation 3.1. It has the advantage over SSFM in that it is globally fourth-order in the step size h , while SSFM is a second-order method. RK4 integrates over z , so for it to be turned into a computational scheme, it still needs a way to deal with the derivatives w.r.t. T , present in the linear operator D . This is again done by transforming D into the frequency domain using an FFT. However, the methods differ in that SSFM uses second-order accurate Strang operator splitting to separate the linear from the nonlinear part of the problem, while RK4IP transforms the problem to the so-called interaction picture to separate the two without approximation. Using RK4 to solve equation 3.1 directly would require 16 FFTs per propagation step. This number can be halved by transforming the problem into the interaction picture [36]. The interaction picture is a representation method, commonly used in quantum mechanics. The method of applying RK4 in the interaction picture is called the *fourth-order Runge-Kutta method in the interaction picture* (RK4IP). RK4IP was first used to solve the Gross-Pitaevskii equation in the study of vortex dynamics in Bose-Einstein condensates [13], an equation similar to the NLSE.

The transformation into the interaction picture is defined as

$$A_I(z, T) := \exp[-(z - z')D(T)] A(z, T), \quad (3.18)$$

where the constant $z' \in \mathbb{R}$ represents the distance between the normal and interaction picture. Differentiating A_I w.r.t. z gives equation 3.1 in the interaction picture

$$\partial_z A_I(z, T) = N_I(A_I(z, T)) A_I(z, T), \quad (3.19)$$

where the nonlinear operator in the interaction picture N_I is defined as

$$N_I(A_I(z, T)) := \exp(-(z - z')D(T)) N(A) \exp((z - z')D(T)). \quad (3.20)$$

By now choosing $z' = z + h/2$, the number of FFTs required per step is halved, due to cancellation of the exponentials with D in equation 3.20 for the midpoint trajectories k_2 and k_3 of RK4, as seen in equation 3.21. Applying RK4 to equation 3.19 yields the following scheme

$$\begin{aligned} A_I &= \exp\left(\frac{h}{2}D\right) A(z, T), \\ k_1 &= \exp\left(\frac{h}{2}D\right) \{h N(A(z, T))\} A(z, T), \\ k_2 &= h N(A_I + k_1/2) \cdot (A_I + k_1/2), \\ k_3 &= h N(A_I + k_2/2) \cdot (A_I + k_2/2), \\ k_4 &= h N\left(\exp\left(\frac{h}{2}D\right) (A_I + k_3)\right) \cdot \exp\left(\frac{h}{2}D\right) (A_I + k_3), \\ A(z + h, T) &= \exp\left(\frac{h}{2}D\right) (A_I + k_1/6 + k_2/3 + k_3/3) + k_4/6. \end{aligned} \quad (3.21)$$

Here, all linear operators D are to be resolved in the frequency domain and all nonlinear operators N in the time domain, similar to SSFM. As said before, in order to do this, we need to perform 8 FFTs per propagation step. This is twice as much as is necessary for SSFM, as can be seen in equation 3.15. However, the fact that RK4IP is a fourth-order method in h and SSFM a second-order method, allows RK4IP to reach a higher accuracy with fewer propagation steps [36].

A possible implementation of RK4IP would be to start with pre-calculating

$$\exp\left(h/2 \cdot \tilde{D}(\omega - \omega_0)\right) \mapsto \tilde{\varphi}_D. \quad (3.22)$$

Here, " \mapsto " means storing the result in a variable. Then, to advance the solution $A^{(j)} := [A(z_j)](T)$ one propagation step, one would perform the following tasks

$$\begin{aligned} \tilde{\varphi}_D \circ \mathcal{F}\{A^{(j)}\} &\mapsto \tilde{A}_I, \\ \tilde{\varphi}_D \circ \mathcal{F}\{h \cdot N(A) \cdot A\} &\mapsto \tilde{k}_1, \\ \mathcal{F}^{-1}\{\tilde{A}_I\} &\mapsto A_I, \quad \mathcal{F}^{-1}\{\tilde{k}_1\} \mapsto k_1, \\ h \cdot N(A_I + k_1/2) \cdot (A_I + k_1/2) &\mapsto k_2, \\ h \cdot N(A_I + k_2/2) \cdot (A_I + k_2/2) &\mapsto k_3, \\ \mathcal{F}\{k_3\} &\mapsto \tilde{k}_3, \quad \mathcal{F}^{-1} \circ \tilde{\varphi}_D(\tilde{A}_I + \tilde{k}_3) \mapsto \alpha, \\ h \cdot N(\alpha) \cdot \alpha &\mapsto k_4, \\ \mathcal{F}^{-1} \circ \tilde{\varphi}_D\left(\tilde{A}_I + \tilde{k}_1/6 + \mathcal{F}\{k_2/3\} + \tilde{k}_3/3\right) + k_4/6 &\mapsto A^{(j+1)}. \end{aligned} \quad (3.23)$$

Here we see how RK4IP can be performed using only 8 FFTs per propagation step. We also note that, although RK4IP requires storing quite a lot of variables (10, to be precise), all variables represent one-dimensional arrays of length N_T , the number of points used to discretise the time window. Since we do not have to store two-dimensional arrays, memory requirements should not be a limitation on modern systems.

3.4 Measure of convergence

In order to investigate the quality of our numerical results and validate our solver, we need a measure for this quality. What this measure looks like depends on whether a reference solution is available or not. In this section, we present two similar measures for investigating the quality of numerical results and therewith the quality of the solver. For the case where a reference solution, analytical or experimental, is available, we present a measure for the error in a numerical solution that can be used to validate the solver by showing convergence to the available reference solution. For the case where there is no reference solution is available, we present a similar measure, but this time for the difference between numerical solutions upon refining simulation parameters. This measure cannot be used to validate the solver, but it can be used to verify its consistency by showing convergence of results. Once

the solver has been verified by showing convergence to a consistent solution, this solution needs to be compared to either a theoretical or an experimental result in order to validate the solution. In addition, we proof that this difference measure is enough to demonstrate the order of convergence of a method.

Note that in this section, we will be writing solutions $[A(z)](T)$ as mappings from the propagation variable z onto the function space $L^2(\Omega)$, i.e., $A : [0, \infty) \rightarrow L^2(\Omega)$, where Ω is the time window that T is an element in. This notation is similar to the one used in section 3.2.

3.4.1 Relative error

When a reference solution, whether analytical or experimental, to a problem is available, e.g., when solving the NLSE with a soliton as an initial condition, the quality of a numerical solution to that problem is given by its deviation from the reference solution. To quantify this, we use the relative error of a numerical solution A_{num} w.r.t. the corresponding analytical solution. The relative error is defined as

$$\epsilon(z) := \frac{\|A_{\text{num}}(z) - A_{\text{ref}}(z)\|_2}{\|A_{\text{ref}}(z)\|_2}, \quad (3.24)$$

Here, A_{ref} is the reference solution and $\|\cdot\|_2$ is the L^2 -norm, defined for a (complex) function $f \in L^2(\Omega)$ as

$$\|f\|_2 := \left(\int_{\Omega} |f(T)|^2 dT \right)^{1/2}. \quad (3.25)$$

The reason for the normalisation is to make the number more insightful, by decoupling its order of magnitude from the size of the solutions. With the above definition, an implementation of a numerical method can be verified by checking that the relative error $\epsilon(z_{\text{max}})$ converges to zero as the simulations are being refined, when using an analytical solution as a reference solution, i.e., that the numerical solution converges to the analytical result. When comparing numerical results to an experimental result, the error of a correct implementation of a numerical method will not converge to zero due to errors in the experimental result and approximations used in the modelling of the problem.

In addition, we can run a sequence of simulations, doubling the number of computational steps used for discretising the interval $(0, z_{\text{max}}]$ for every consecutive simulation (i.e., halving the step size). As will be derived in subsection 3.4.2, the slope of $\epsilon(z_{\text{max}})$ w.r.t. an analytical solution plotted against the number of computational steps on a log-log scale should converge to minus the order of convergence of the method used.

3.4.2 Relative difference

When there is no analytical solution available to the problem that is being solved numerically, e.g., for almost all cases when solving the GNLSE, it is less straightforward to investigate the quality of a numerical solution. One tool that can be used to study the convergence of such a solution w.r.t. various simulation parameters is the relative difference between solutions. Suppose we are solving a problem using a sequence of more and more accurate simulation parameters (e.g., propagation step sizes, time window sizes). We then get a sequence of approximate solutions $\{A_j\}_{j=1}^n$. We define the relative difference between solutions in the sequence as follows.

$$\delta_j(z) := \frac{\|A_{j+1}(z) - A_j(z)\|_2}{\|A_n(z)\|_2} \longrightarrow 0 \quad \text{as } j \longrightarrow \infty \quad \text{for all } z > 0. \quad (3.26)$$

This is also our requirement for convergence w.r.t. the simulation parameter that is being varied.

Suppose we are calculating propagation of $[A_j(z)](T)$ for $z \in (0, z_{\max}]$ and T in some window Ω . Suppose further that we are refining our grid by doubling the amount of computational steps N_z , used to discretise $(0, z_{\max}]$, every time, i.e., $N_z = N_{z,0} \cdot 2^j$ for $j \in \{1 \dots n\}$. We then write the step size as

$$h_j = \frac{z_{\max}}{N_{z,0} \cdot 2^j} \quad (3.27)$$

Additionally, suppose A_j converges to some function A , i.e., $A_j \rightarrow A$ as $j \rightarrow \infty$, with order of convergence p , i.e.,

$$A_j = A + C_1 \cdot h_j^p + \mathcal{O}(h_j^{p+1}), \quad (3.28)$$

where C_1 does not depend on j , but possibly on T . Neglecting the higher-order terms and using equation 3.27, we then have that

$$\begin{aligned} A_{j+1} - A_j &= A - A + C_1 \cdot (h_{j+1}^p - h_j^p) \\ &= C_1 \cdot \frac{z_{\max}^p}{N_{z,0}^p} \left[\frac{1}{2^{(j+1)p}} - \frac{1}{2^{jp}} \right] \\ &= C_1 \cdot \frac{z_{\max}^p}{N_{z,0}^p} \left(\frac{1}{2} \right)^{jp} \left(\frac{1}{2^p} - 1 \right) \\ &= A_{j+1} - A_j = C_2 (1/2)^{jp}, \end{aligned} \quad (3.29)$$

where, again, C_2 does not depend on j , but possibly on T . Then we finally have

$$\delta_j(z) = \frac{\|A_{j+1}(z) - A_j(z)\|_2}{\|A_n(z)\|_2} = \frac{\|C_2\|_2}{\|A_n(z)\|_2} \cdot \left| (1/2)^{jp} \right| = C (1/2)^{jp}. \quad (3.30)$$

This allows us to verify the order of convergence without the need for an analytic solution. When we plot δ against the number of computational steps in a logarithmic fashion, we observe that

$$\frac{\partial [\log \delta_j(z)]}{\partial [\log N_z]} = \frac{\partial [\log C - jp \log 2]}{\partial [j \log 2]} = -p, \quad (3.31)$$

since C is independent of j . In other words, When we plot δ against the number of computational steps in a log-log plot, the slope of the curve should equal minus the order of convergence. The same holds for the relative error ϵ , as defined in equation 3.24.

Chapter 4

Predicting nonlinear pulse propagation

In this chapter, we first provide validation for our implementation of the methods described in sections 3.2 and 3.3, by analysing particular solutions to the NLSE and the GNLSE, both qualitatively and quantitatively. These solutions are obtained using the material properties of a photonic crystal fiber, we start by declaring and analysing these properties. We show that the features seen in the results agree qualitatively with what one would expect from a physics point of view; we validate the results quantitatively through comparison with theoretical results from chapter 2.

Secondly, we provide verification for our implementation by verifying the convergence of results w.r.t. various numerical parameters, employing the methods from section 3.4. In addition, we determine the order of convergence at which results converge w.r.t. the number of computational steps and compare this to statements in chapter 3 for SSFM and RK4IP. In addition, we make a comparison between the relation of accuracy to the number of computational steps and computation time for the two methods.

Finally, we use the GNLSE to simulate supercontinuum generation in a photonic crystal fiber. We present the effect of spectral broadening due to nonlinear propagation for various pulse energies.

4.1 Nonlinear Schrödinger Equation

In this section, we present various results of solving the NLSE with the methods described in chapter 3, namely SSFM and RK4IP. We show propagation of a Gaussian pulse and N th-order solitons with integer and non-integer N and discuss the asymptotic behaviour of these pulses w.r.t. the propagation distance. In

addition, we provide verification for our implementation of the methods, by showing convergence of the relative error w.r.t. analytical solutions, with the expected order of convergence.

4.1.1 Pulse propagation

Here, we present the results of solving the NLSE, as seen in equation 2.18, with anomalous GVD, i.e., $\text{sgn}(\beta_2) = -1$, using our implementation of SSFM and RK4IP, as seen in equation 3.15 and 3.23, respectively. First, we check the unchanging propagation of a fundamental soliton. The results of solving the NLSE with RK4IP, taking as initial conditions a fundamental soliton, i.e., $u(0, \tau) = \text{sech}(\tau)$ and using numerical parameters $N_\tau = 8192$, $N_\xi = 8192$ and $\tau_{\max} = 80.0$, can be seen in figure 4.1. It shows a comparison of the calculated pulse shape with a fundamental soliton, i.e., a hyperbolic secant in the time domain, which is the analytical solution, as a fundamental soliton propagates without changing its shape. We see, qualitatively, that the simulation results agree very well with this prediction for RK4IP. The same holds for SSFM. We will later discuss the analysis of the fundamental soliton case more quantitatively.

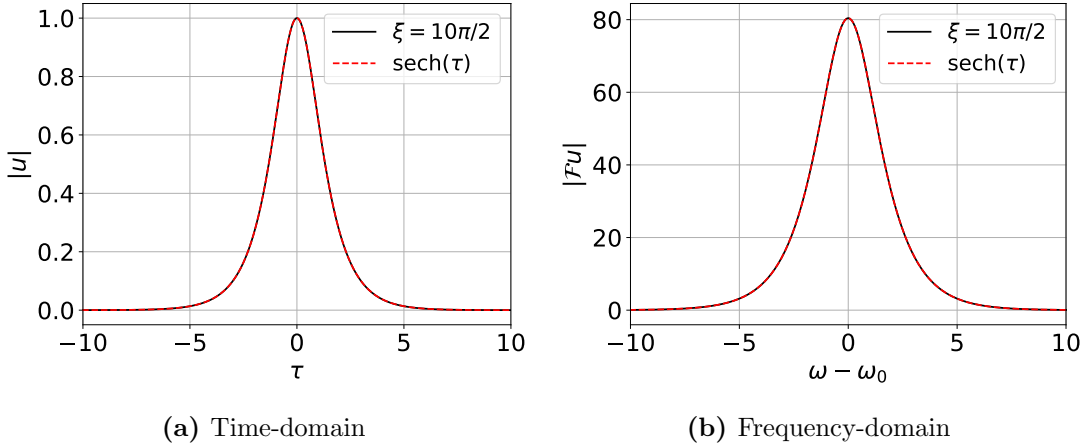


Figure 4.1: Pulse shape of a soliton after propagation over $\xi \in (0, 10\pi/2]$ in the (a) time and (b) frequency domain. The black curves show the solution, calculated using RK4IP, the red curves show a hyperbolic secant shape and its spectrum, i.e., a fundamental soliton.

The first interesting case we consider is the propagation of a 2nd-order soliton $u_{\text{sol}}^{(2)}(\xi, \tau)$ over $\xi \in (0, \xi_{\max}]$, using initial conditions from equation 2.26 and $N = 2$. To clearly show the periodic behaviour associated with higher-order soliton propagation, both in the time and frequency domain, we take ξ_{\max} equal to 10 periods, i.e., $\xi_{\max} = 10\pi/2$. The resulting intensity $I = |u_{\text{sol}}^{(2)}|^2$ can be seen in figure 4.2, in the time and frequency domain. These results were obtained by solving the NLSE with RK4IP, using computational steps $N_\xi = 8192$ and time window points $N_\tau = 8192$ as well and a time window size of $\tau \in [-\tau_{\max}, \tau_{\max}]$, $\tau_{\max} =$

80.0. Remember we use a comoving frame, propagating at the group velocity β_1^{-1} . We discuss the choice of numerical parameters in section 4.2.4 and we show convergence w.r.t. N_ξ in section 4.1.2. Furthermore, the frequency range for the angular frequency around the carrier frequency ω_0 is defined through $\omega - \omega_0 \in [-\omega_{\max}, \omega_{\max}]$, $\omega_{\max} := \pi N_\tau / 2\tau_{\max}$, as per the Nyquist-Shannon sampling theorem [51]. Figure 4.2 shows the periodic propagation of a second-order soliton with soliton period $\xi_0 = \pi/2$, as the theory in section 2.1.3 predicts. Note the coincidence of temporal broadening and spectral narrowing and vice versa. This periodic motion is the result of interplay between self-phase modulation and GVD [4, chapter 5].

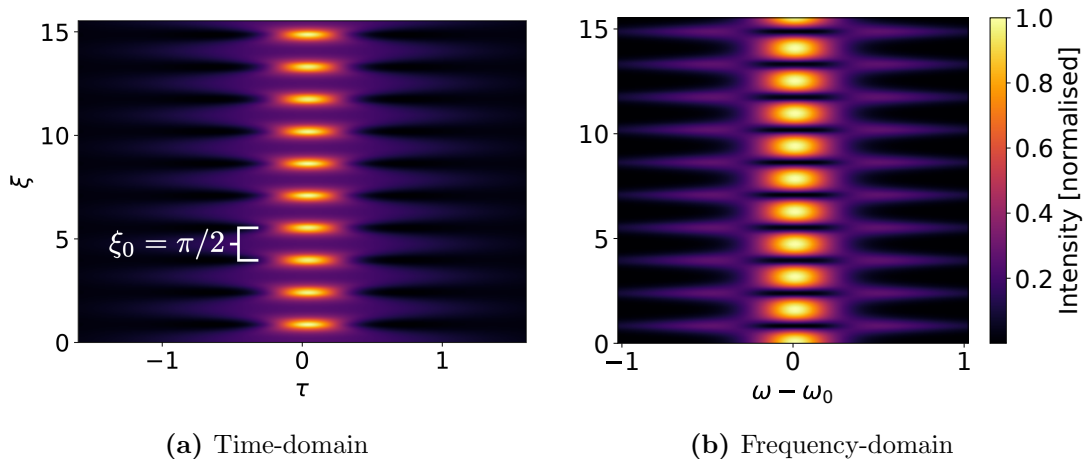


Figure 4.2: Propagation of a second-order soliton with $\xi_{\max} = 10\pi/2$. The images show the normalised intensity in the (a) time and (b) frequency domain.

At this point, we recall that the dimensionless system solved here solely depends on N and $\text{sgn}(\beta_2)$, where N is defined as

$$N^2 = \frac{L_D}{L_{NL}} = \frac{T_0^2 \gamma P_0}{|\beta_2|}, \quad (4.1)$$

with the nonlinear parameter γ and GVD $|\beta_2|$ as system parameters and the pulse width T_0 and peak power P_0 as input pulse parameters. Thus, a specific solution of the dimensionless NLSE describes the behaviour of many different pulses propagating through many different system, for which these four parameters obey equation 4.1. For example, a system will show identical behaviour, in the dimensionless picture, to that of a system with identical γ and P_0 , but with twice the pulse width and a GVD that is four times as strong. Similarly, doubling the peak power and halving the nonlinear parameter leaves the system behaviour unaltered. Finally, note that N increases linearly with P_0 and thus with the field amplitude squared, just as with the pulse width. This means that doubling the pulse amplitude and halving its width leaves its behaviour unaffected in the dimensionless picture.

Analytical solutions exist for solitons with integer N . This is not the case for almost any other input pulse. It is for these cases that we need numerical solutions

to study their behaviour upon nonlinear propagation through a medium. The first example of such input pulses are hyperbolic secant shaped pulses, as given by equation 2.26, with non-integer \tilde{N} . As discussed in section 2.1.3, such a pulse is transformed into a soliton pulse of order N , for which N is the closest integer to \tilde{N} . Examples of this can be seen in figures 4.5 and 4.3 for $\tilde{N} = 1.6$ and figure 4.4 for $\tilde{N} = 1.1$. Figures were made using $\tau_{\max} = 80.0$, $N_{\tau} = 8192$ and $N_{\xi} = 8192$.

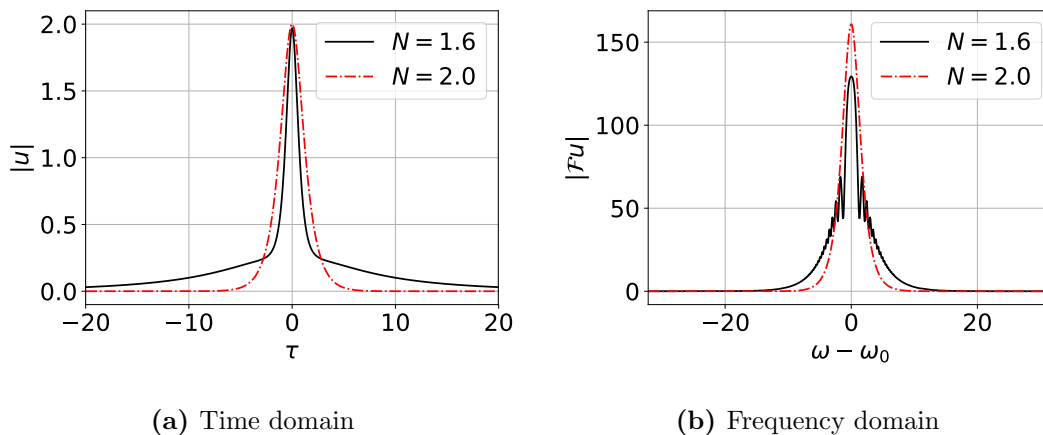


Figure 4.3: Comparison of pulses after propagation in the (a) time and (b) frequency domain, with $\xi_{\max} = 10\pi/2$. The propagation is continued from that shown in figure 4.5

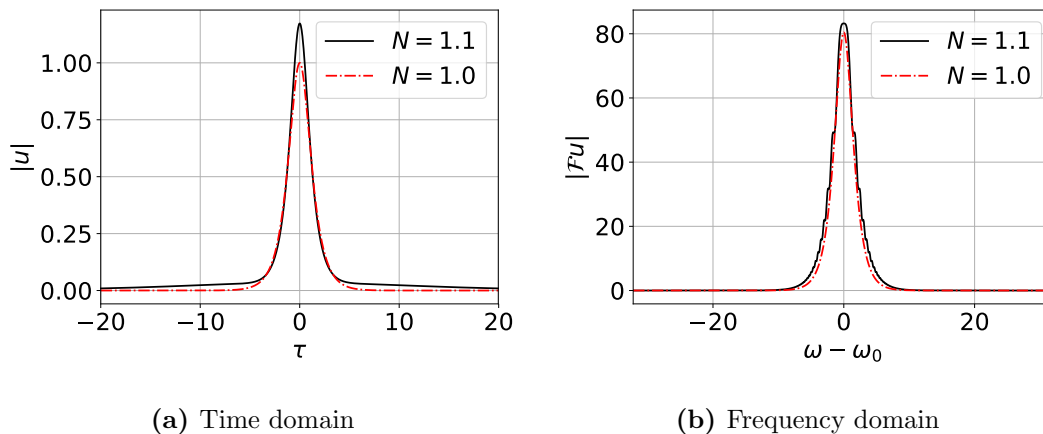


Figure 4.4: Comparison of pulses, one with $\tilde{N} = 1.1$, one with $N = 1.0$, after propagation with $\xi_{\max} = 10\pi/2$ in the (a) time and (b) frequency domain.

We find that the soliton period ξ_0 does not equal $\pi/2$ for $\tilde{N} = 1.6$, as can be seen in figure 4.5c. This seems to be the case for all hyperbolic secant pulses with non-integer N . Looking at figures 4.3 and 4.4, we see how the convergence of the non-integer hyperbolic secant pulse to an integer-order soliton looks after ten soliton periods for $\tilde{N} = 1.6$ to $N = 2.0$ and $\tilde{N} = 1.1$ to $N = 1.0$, respectively. We observe that convergence seems to be much faster for $\tilde{N} = 1.1$ than for $\tilde{N} = 1.6$. The surplus energy is emitted in the form of continuum radiation and is visible

in the wings of the pulse in figures 4.3a and 4.4a. Further, we see in figure 4.4a that the $\tilde{N} = 1.1$ pulse has already narrowed down to the pulse width of the fundamental soliton, while the $\tilde{N} = 1.6$ pulse in figure 4.3a does not seem close to having converged to its theoretical, asymptotic solution. The sharpening observed for $\tilde{N} = 1.1$ is in agreement with the theory, that convergence to a soliton of lower order leads to sharpening, while convergence to a soliton of higher order leads to broadening [4, chapter 5]. Our hypothesis is that these hyperbolic secant pulses

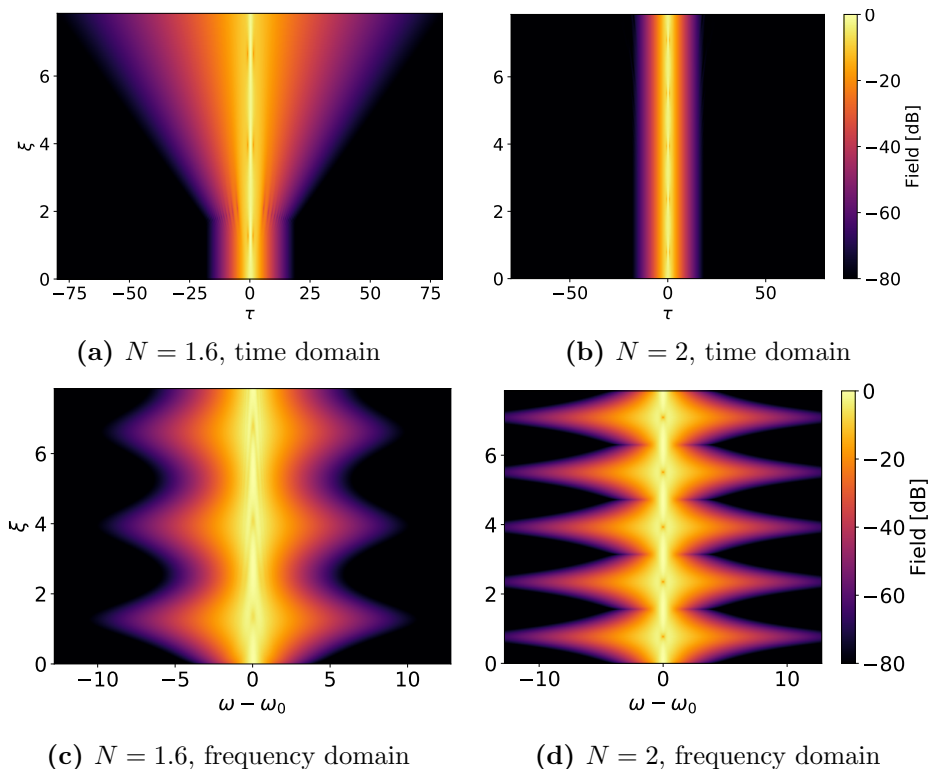
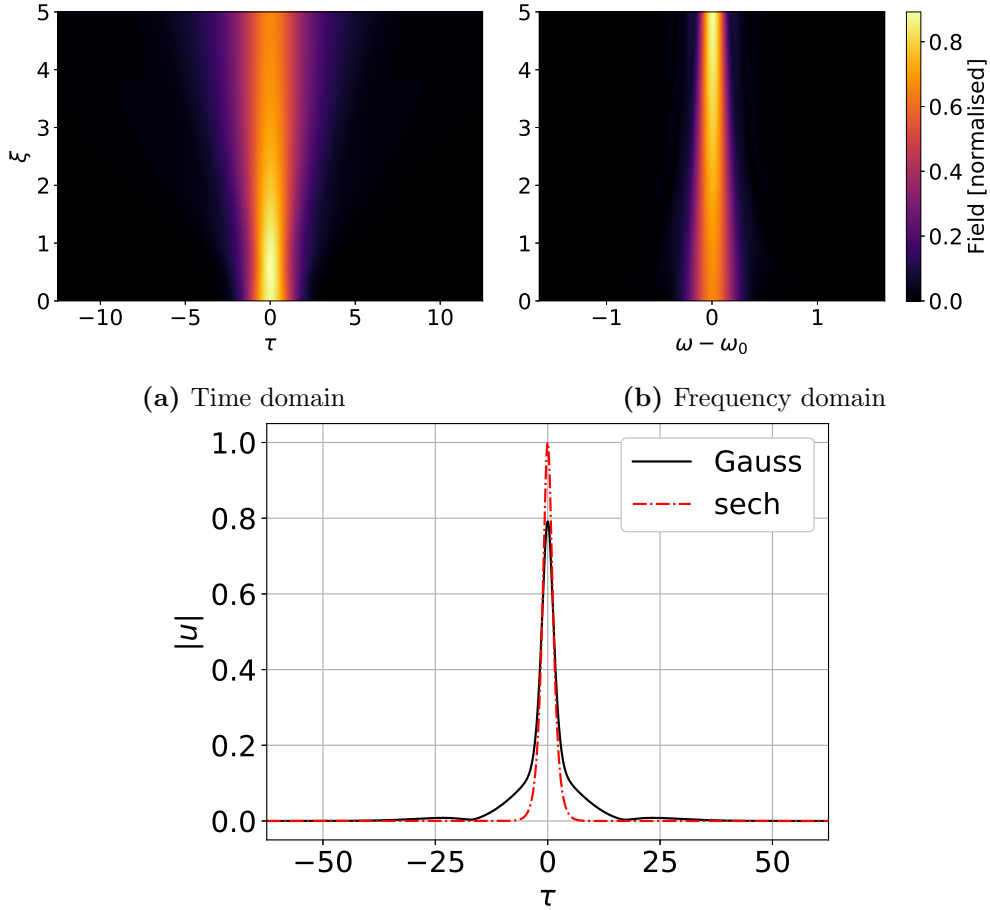


Figure 4.5: Propagation of two solitons with $\xi_{\max} = 5\pi/2$ in the time and frequency domain on a logarithmic scale, (a,c) one with $\tilde{N} = 1.6$, (b,d) one with $N = 2.0$.

converge to solitons in the non-normalised picture. However, since the pulse width and amplitude are altered and the pulse is still normalised with the original pulse width and amplitude, the resulting stable soliton does not show as an integer N soliton in the normalised picture. Furthermore, since the pulse width is altered, the dispersion length L_D , used to normalise the propagation distance, is also incorrect. If we were to renormalise the resulting pulse, we expect to find a soliton period of $\xi_0 = \pi/2$ again.

The last result from the NLSE we will be discussing can be seen in figure 4.6. It shows the propagation of the field when using a Gaussian pulse as initial condition, i.e., $u(0, \tau) = \exp(-\tau^2)$. The figure was obtained with $\xi_{\max} = 5$, $\tau_{\max} = 250$, $N_\xi = 16384$ and $N_\tau = 16384$ (although these time window size and number of computational steps in both directions could probably be relaxed without compromising the accuracy of the result. We discuss the choice of numerical parameters in section 4.2.4). In figures 4.6a and 4.6b, we see that the pulse broadens in the



(c) Comparison of the pulse after propagation with a hyperbolic secant.

Figure 4.6: Propagation of a Gaussian pulse with $\xi_{\max} = 5$ and peak power equal to unity, according to the NLSE. In the plot we see the normalised amplitude of the field in the (a) time and (b) frequency domain. In (c) we see a comparison of the pulse shape at $\xi = 10$ with a hyperbolic secant.

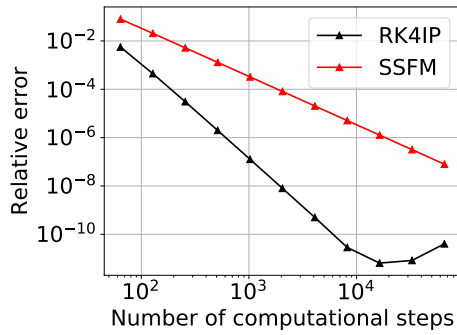
time domain and correspondingly narrows in the frequency domain. Also, in the time domain plot, we see that the peak power first rises ever so slightly, before decreasing in a monotone fashion. In addition, figure 4.6c shows that the pulse seems to converge to a hyperbolic secant shape, but with a different amplitude than the fundamental soliton and with a part that broadens away from the pulse center, as the pulse propagates. These observations are the same as the ones done by Agrawal for the same simulation setup [4, chapter 4].

4.1.2 Convergence with respect to analytical solutions

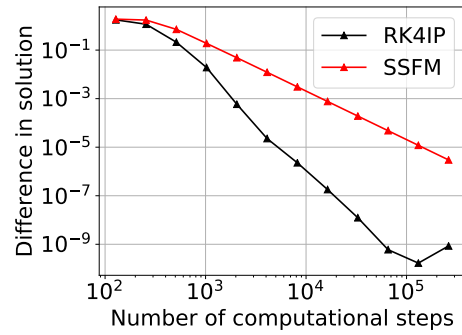
In section 3.4, we introduced a quantitative way of verifying our numerical results. Here, we use the relative error from equation 3.24 to investigate the numerical error in our solutions and the convergence of this error w.r.t. the number of computational steps N_ξ . In order to be able to do this, we need a reliable reference solution. We consider two cases of soliton propagation, with $N \in \{1, 2\}$ and analytical solutions as seen in equations 2.24a and 2.25, respectively, which serve as reference solutions. The two solitons were propagated with $\xi_{\max} = 10\pi/2$, $\tau_{\max} = 80.0$, $N_\tau = 8192$ using both SSFM and RK4IP. To verify the correct order of convergence, the relative error of the pulse after propagation w.r.t. the analytical solution is plotted against the number of computational steps in a log-log plot in figure 4.7. The order of convergence p is equal to minus the slope of the graphs, as was shown in equation 3.31. We can see in figures 4.7a and 4.7b that $p = 2$ for SSFM and $p = 4$ for RK4IP, for both solitons, until an error of the order of the machine precision is reached. This agrees with the orders of convergence we expect for SSFM and RK4IP, as discussed in sections 3.2 and 3.3, respectively. Also, we observe from figure 4.7b that roughly an order of magnitude more computational steps are required to reach the same accuracy for the second-order soliton as for the first-order soliton. This rapid increase in computational effort as the complexity of the problem increases, is the reason higher-order methods are interesting for solving the NLSE and even more so for the GNLSE.

In addition, in figure 4.7c we see the same relative errors for $N = 2$, but here plotted against the computational time¹. This figure shows that RK4IP not only converges faster than SSFM, but also achieves a higher accuracy for the same computational time. That a higher order of convergence results in an increased computational efficiency, even for large step sizes, is not entirely obvious, as the RK4IP uses 8 FFTs and more operations per propagation step, while SSFM uses 4 FFTs, as was shown in sections 3.2 and 3.3. Thus, RK4IP is the preferred method, as it reaches a higher accuracy with lower computational time. Also, since it is a higher-order method than SSFM, its computational time scales better for higher accuracies than SSFM. This makes RK4IP especially suitable for more complex

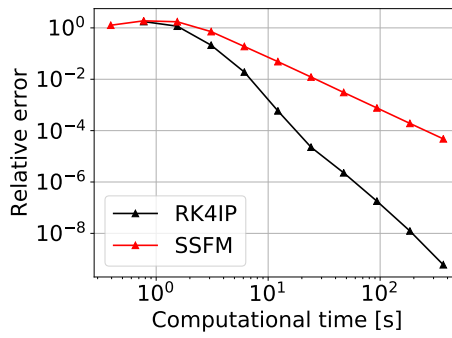
¹The computational time was measured using the function `perf_counter` from Python's `time` module [3]. Note that this function measures wall time, not cpu time. All timed simulations were run on a dedicated machine, to prevent inclusion of background processes in the measured computational time.



(a) fundamental soliton



(b) second-order soliton



(c) second-order soliton

Figure 4.7: Relative error as a function of the number of computational steps for (a) a fundamental and (b) a second order soliton for both SSFM (red line) and RK4IP (black line), and (c) as a function of the computational time for the second order soliton, again for both methods. All graphs show 4th (2nd) order convergence for RK4IP (SSFM), respectively. In all cases, $\xi_{\max} = 10\pi/2$.

cases with higher pulse energies and higher orders of dispersion, as these cases require a much higher accuracy in order to correctly model all the relevant features [18]. Unless otherwise specified, we use RK4IP method in the remainder of this work.

4.2 Generalised Nonlinear Schrödinger Equation

The NLSE is an interesting topic of research, since its relative simplicity allows for insightful, theoretical results. However, the assumptions necessary in its derivation, as discussed in section 2.1.1, are quite restrictive. Especially the narrowband approach, i.e., $\Delta\omega \ll \omega_0$, means the NLSE is not adequate for modelling higher-intensity pulses undergoing extreme spectral broadening. The GNLSE extends the spectral relevance of the NLSE by including higher-order dispersive effects.

In this section, we present the results of solving the GNLSE, for theoretically relevant cases, with the methods described in chapter 3, namely SSFM and RK4IP. We show propagation of a fundamental soliton under the influence of third-order dispersion, soliton fission for a second-order soliton under the influence of higher-order dispersion and spectral broadening of a more realistic Gaussian pulse with varying intensities, simulating the generation of a supercontinuum. We compare these results with theoretical results from section 2.2, in order to validate our implementation of the methods. In addition, we verify the convergence of these methods using the method presented in section 3.4.2 and we discuss strategies for finding efficient numerical parameters.

4.2.1 Material properties

All the results in this section are obtained using the dispersion data from a photonic crystal fiber (PCF). The dispersion data for this PCF is given as a series of polynomial coefficients β_k , as defined in equation 2.12, for $k \in \{1 \dots 13\}$, which describe $\beta(\omega)$ as a Taylor polynomial around the carrier (angular) frequency ω_0 . The carrier wavelength for this PCF is 800 nm, which corresponds to a frequency of around 374.74 THz. The β_k can be seen in table 4.1, together with the nonlinear index n_2 and the effective mode area A_{eff} , which are assumed to be independent of frequency, as discussed in section 2.1.1, and determined at the carrier frequency. We notice that β_k goes to zero rather quickly as k grows. This begs the question, is there a point of including thirteen orders of dispersion? For relatively narrowband pulses, these higher-order terms are indeed negligible. If we compare, for instance, the contribution of the tenth-order term in the Taylor expansion of β with β_0 , i.e., stating that $\beta_0 = \beta_{10} (\omega - \omega_0)^{10}/10!$, we find that this expression is satisfied for $(\omega - \omega_0) = 2857$ THz or $(f - f_0) = 454.7$ THz. A spectral width in the order of hundreds of THz is not unusual in the study of supercontinuum generation [21]. The propagation constant β , GVD and integrated dispersion β_{int} as a function of

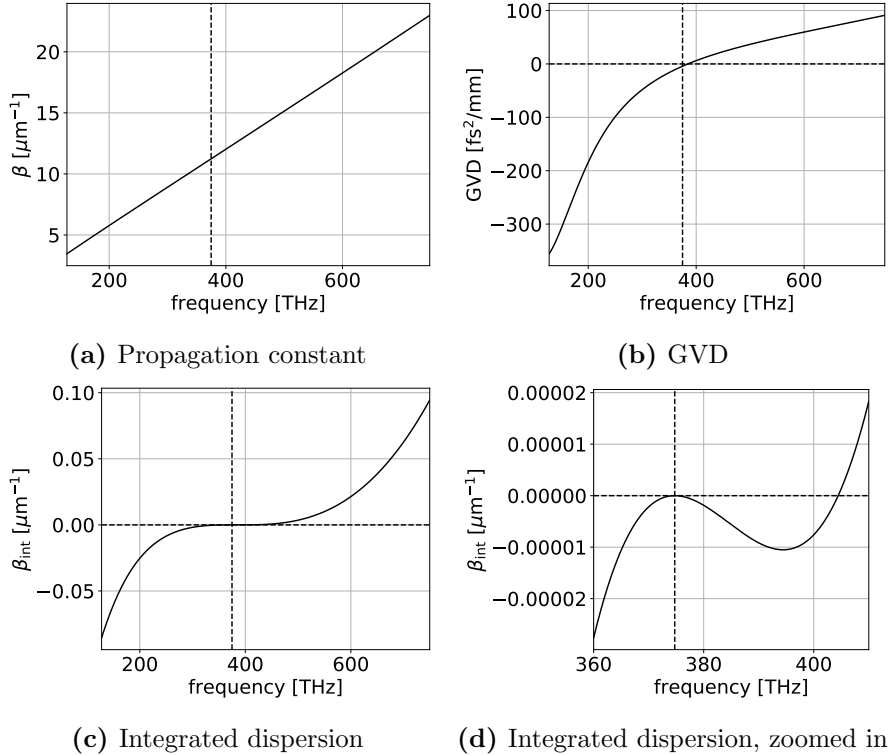


Figure 4.8: The (a) propagation constant β , (b) GVD and (c,d) integrated dispersion β_{int} of the PCF used for the simulations in this section, plotted against frequency with carrier frequency $f_0 = 374.74$ THz.

frequency are shown in figure 4.8, for the wavelength range $\lambda \in [400, 2350]$ nm. This is the range for which most optical fibers are transparent [58]. Remember that β_{int} is defined as in equation 2.41. The PCF was designed for SCG at a carrier wavelength of $\lambda_0 = 800$ nm. This is reflected in the fact that λ_0 lies very close to a zero dispersion wavelength (ZDW), a wavelength for which the GVD equals zero, as can be seen in figure 4.8b. Being close to a ZDW means the GVD is very low, which allows a pulse to retain its shape for a longer period of time as it propagates, giving the nonlinear processes more time to affect the pulse. In section 2.2.3, we discussed the relevance of β_{int} , in that its roots are an approximation to the frequencies that are phase-matched to solitons, centered at the carrier frequency. This PCF has one phase-matched frequency in the relevant frequency range, which is at 404.4 THz. This root is made visible in figure 4.8d.

4.2.2 Comparison of results with theory

Now that we have our dispersion data, we can start solving the GNLSE and comparing results with theory. The first step is simulating the propagation of a fundamental soliton under the influence of only second-order dispersion, i.e., GVD, and third-order dispersion. Thus we use β_2 and β_3 from table 4.1 and set $\beta_k = 0$ for $k > 3$. We choose this system, since there is a theoretical result available for

β_0	11236444.5915148 1 m ⁻¹	β_8	$-4.29164976784012 \cdot 10^{-114}$ s ⁸ m ⁻¹
β_1	$4.95001710231803 \cdot 10^{-9}$ s m ⁻¹	β_9	$5.96596747061804 \cdot 10^{-129}$ s ⁹ m ⁻¹
β_2	$-4.20056799728266 \cdot 10^{-27}$ s ² m ⁻¹	β_{10}	$6.86896184496321 \cdot 10^{-143}$ s ¹⁰ m ⁻¹
β_3	$7.06952086512158 \cdot 10^{-41}$ s ³ m ⁻¹	β_{11}	$-4.65289497284061 \cdot 10^{-157}$ s ¹¹ m ⁻¹
β_4	$-7.21188988183953 \cdot 10^{-56}$ s ⁴ m ⁻¹	β_{12}	$1.25474042542014 \cdot 10^{-171}$ s ¹² m ⁻¹
β_5	$1.25000246903091 \cdot 10^{-70}$ s ⁵ m ⁻¹	β_{13}	$-1.34604444802229 \cdot 10^{-186}$ s ¹³ m ⁻¹
β_6	$-2.33838474999689 \cdot 10^{-85}$ s ⁶ m ⁻¹	n_2	$3.2 \cdot 10^{-20}$ m ² W ⁻¹
β_7	$9.02919203762881 \cdot 10^{-100}$ s ⁷ m ⁻¹	A_{eff}	$1.0 \cdot 10^{-12}$ m ²

Table 4.1: Dispersion data, nonlinear index n_2 and effective mode area A_{eff} for the PCF used for the results in this section. Dispersion data is courtesy of Niklas Lüpken, from the Optische Technologien group from the university of Münster.

it that we can compare our results with, in the form of equation 2.31. As initial condition we use a soliton pulse, i.e., $A_{\text{sol}}^{(N)}(0, T) = \sqrt{P_0} \cdot \text{sech}(T/T_0)$, with pulse width $T_0 = 60$ fs. Since we are considering a fundamental soliton, we get the pulse peak power by setting $N = 1$ in equation 4.1. We then get $P_0 = N^2 |\beta_2| / \gamma T_0^2 \approx 4.64$ W and a total pulse energy of

$$E \left[A_{\text{sol}}^{(1)}(z, \cdot) \right] := \int_{\mathbb{R}} \left| A_{\text{sol}}^{(1)}(z, T') \right|^2 dT' = 0.56 \text{ pJ}. \quad (4.2)$$

To get an idea of the typical length scales over which the dispersive and nonlinear effects will take place for this system, we calculate L_D and L_{NL} , which are nearly identical at 85.70 cm. The pulse was propagated over $z \in (0, z_{\text{max}}]$, with $z_{\text{max}} = 400$ m (this was quite excessive). The time window was chosen at $T \in [-T_{\text{max}}, T_{\text{max}}]$, with $T_{\text{max}} = 31$ ps. Furthermore, the number of computational steps $N_z = 4096$ and samples in the time window $N_T = 4000$ were used. The results can be seen in figure 4.9. The figure clearly shows the relatively unperturbed propagation of the fundamental soliton, apart from a change in its group velocity. The presence of third-order dispersion lowers the group velocity, which is manifested as a drift through the frame, that still propagates at the original group velocity β_1^{-1} . This behaviour is as predicted by the theory, described in section 2.2.1, apart from a slight, asymmetric change in the pulse shape (not visible in the figure). The total temporal drift of the soliton observed in the figure is $T_s(400 \text{ m}) = 1.310$ ps, which agrees remarkably well with the theoretical value of 1.309 ps, obtained using equation 2.31.

Next is the simulation of fission of a second-order soliton under the influence of higher-order dispersion, in this case up to thirteenth order, $\beta_k = 0$ for $k > 13$. As initial condition we use $A_{\text{sol}}^{(2)}(0, T)$ with $P_0 = 2^2 |\beta_2| / \gamma T_0^2 \approx 18.57$ W, $T_0 = 60$ fs and therefore pulse energy $E[A_{\text{sol}}^{(2)}] = 2.23$ pJ. The pulse shapes in the time domain for $z = 1.5$ m and $z = 5.0$ m can be seen in figures 4.10c and 4.10d, respectively. The results for $T_{\text{max}} = 10$ ps, $z_{\text{max}} = 5.0$ m, $N_T = 8192$ and $N_z = 8192$ can be seen in figures 4.10a and 4.10b. In figure 4.10a, we can clearly see the second-order soliton propagate for a short distance, before the weak binding is broken by the higher-order dispersion and it splits into two stable fundamental solitons and some dispersive wave. In Figure 4.10b, we see the broadening of the spectrum that

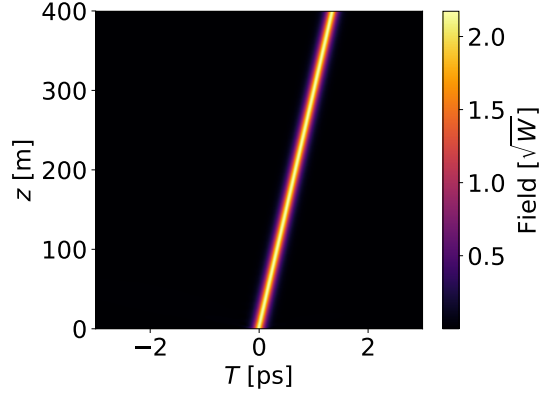


Figure 4.9: A fundamental soliton undergoing a temporal drift due to third-order dispersion.

happens during the fission, until the spectrum spans almost 100 THz at the -30 dB level. Looking at figures 4.10d and 4.10c, we can see that the second-order soliton

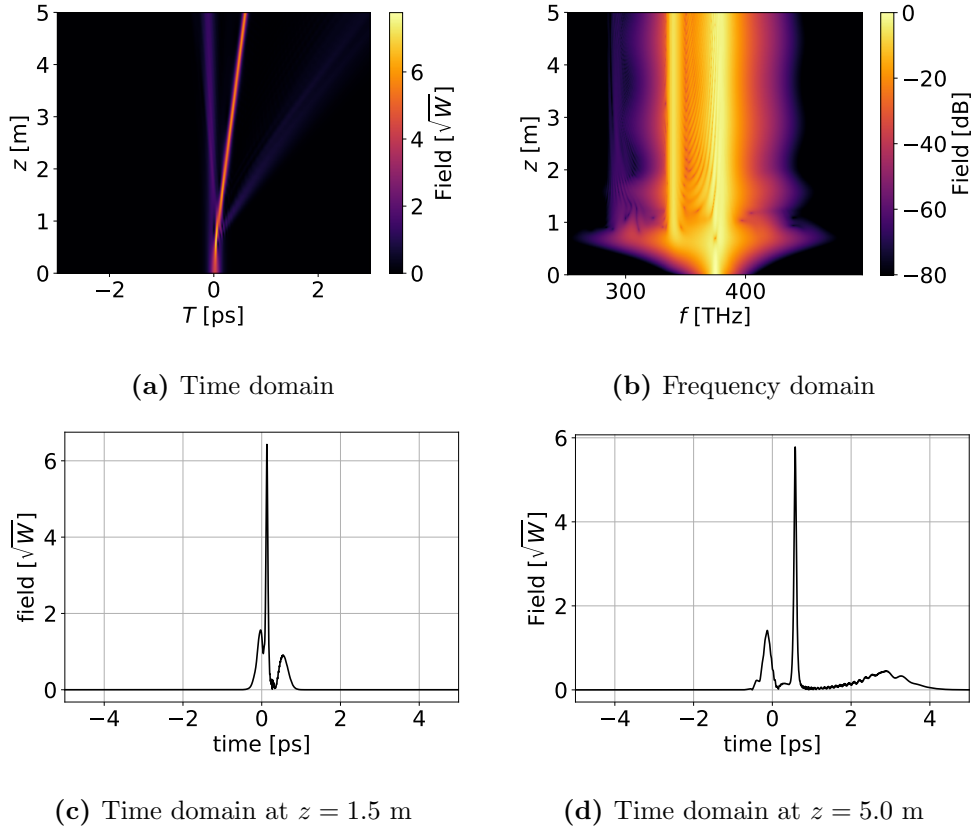


Figure 4.10: Break-up of a second-order soliton into two fundamental solitons and a dispersion wave due to higher-order dispersion. In (c,d), we see the pulse at $z = 1.5$ m and $z = 5.0$ m, respectively.

has split into two fundamental soliton pulses, which is in agreement with the theory from section 2.2.2. See table 4.2 for the pulse widths T_k and peak powers P_k observed in figure 4.10 and predicted by equation 2.33. We notice that the

	T_1 [fs]	T_2 [fs]	P_1 [W]	P_2 [W]
Simulated at $z = 1.5$ m	20.34	68.4	41.32	2.452
Simulated at $z = 5.0$ m	25.5	116	33.40	1.308
Predicted by theory	20.0	60.0	41.78	4.643

Table 4.2: Pulse widths T_k and peak powers P_k for the two fundamental solitons created by soliton fission, as seen in figure 4.10 and predicted by equation 2.33.

simulated results agree reasonably well with the expected value at $z = 1.5$ m, especially for the first soliton, i.e., $k = 1$. However, less so at $z = 5.0$ m. This is not surprising, since equation 2.33 is an approximate result, in that these theoretically expected widths and peaks are for the resulting fundamental solitons at the moment of fission. Because we are including higher-order dispersion, the widths and peaks of these solitons are affected during propagation. Agrawal shows measurement results, in which the pulse width is measured as a function of the propagation distance. It shows that the pulse width sharply drops during soliton fission, but steadily rises again afterwards due to GVD not being completely cancelled by SPM under the influence of higher-order dispersion [4, chapter 12]. This explains the relatively small deviation from the expected values at $z = 1.5$ m and the larger deviation at $z = 5.0$ m.

4.2.3 Convergence of numerical solutions

In section 3.4.2, we presented a method to quantitatively investigate convergence of results w.r.t. any parameter. In the case when a reference solution for the GNLSE is not readily available, like the analytical solutions for the NLSE, we can still show the order at which methods converge w.r.t. the number of computational steps N_z . As was discussed in section 3.4.2, this involves plotting the relative difference between solutions $\delta(z_{\max})$ against N_z in a log-log plot. This result can be seen in figure 4.11 for the propagation of a second-order soliton with pulse width and peak power identical to the one that was used in section 4.2, with $z_{\max} = 1.3$ m, $T_{\max} = 10$ ps and $N_T = 2048$. Similar to the NLSE, this figure shows 2nd-order convergence for SSFM and 4th-order for RK4IP, until machine precision limits further convergence.

In a similar manner, convergence w.r.t. the order of dispersion can be verified. This was done by solving the GNLSE using again the same second-order soliton as initial condition, but now taking orders of dispersion up to $k \in 2..13$, using the dispersion data from a photonic crystal fiber as shown in table 4.1. This time plotting $\delta(z_{\max})$ against k gives figure 4.12. Similar convergence checks have been performed to check convergence w.r.t. the time window size T_{\max} and the number of samples in the time window N_T . It is necessary that results converge in all cases, since the numerical results are not approximating a consistent answer if this is not the case. Therefore, showing convergence is the first step towards verifying convergence of our implementation.

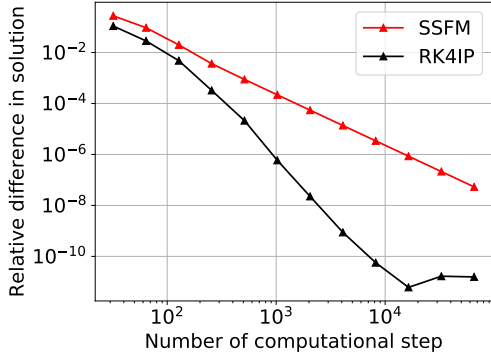


Figure 4.11: Relative, normed difference $\delta(z_{\max})$ plotted against the number of computational steps N_z for both SSFM (red line) and RK4IP (black line). The simulations concern the propagation of a second-order soliton with $z_{\max} = 1.3$ m. This plot shows (4th-) 2nd-order convergence for the (RK4IP) SSFM, respectively.

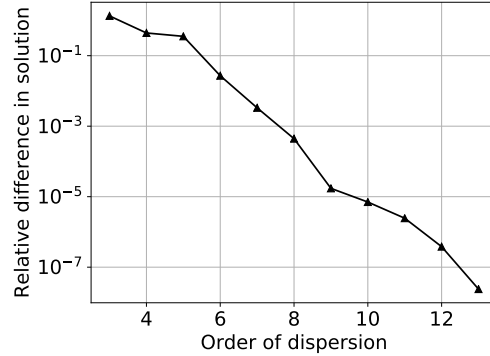


Figure 4.12: Relative, normed difference $\delta(z_{\max})$ plotted against the order of dispersion for the propagation of a second-order soliton, with $z_{\max} = 3$ m. This plot shows convergence of the result w.r.t. the order of dispersion.

4.2.4 Determining suitable numerical parameters

While a convergence plot, obtained in the previous subsection, might give us an idea of the size of the numerical error, it is not sufficient if our goal is to produce a graph without any visible errors, while minimising calculation time. In order to produce these graphs needed to compare results with theory, sweeps were performed over all the relevant numerical parameters, namely the number of computational steps N_z , the number of samples in the time domain N_T and the time window size T_{\max} . The goal here is to find a set of parameters that leads to a result without any numerical artifacts, such that all visible feature are guaranteed to be physical. This is the case, when the part of the spectrum that depends on N_z has disappeared.

The width of the frequency window is determined by the sampling rate in the time domain and thus by N_T , according to the Nyquist–Shannon sampling theorem [51], as was discussed earlier. Therefore, N_T was taken as the least amount of samples for which the pulse spectrum fits in the frequency window reasonably well. In other words, such that the part of the spectrum outside of the frequency window has at least dropped to -40 dB w.r.t the peak of the spectrum. An illustration of this is depicted in figure 4.13. Here, we see the resulting spectrum from simulating the propagation of a Gaussian pulse with $P_0 = 100$ W, $T_0 = 60$ fs and $z_{\max} = 6.73$ m. Also, $T_{\max} = 25$ ps and $N_z = 8192$ were set and N_T was chosen such that the spectrum had fallen to below -40 dB at the edge of the spectral window, which is the case at $N_T = 16384$, as can be seen in the figure. Note that a part of the spectrum does fall outside of the spectral window. However, this part of the spectrum is purely a numerical artefact, as will become clear when we discuss the

dependence on N_z and can be seen in figure 4.14. Similarly, the ideal value for T_{\max} was determined by the width of the pulse in the time-domain.

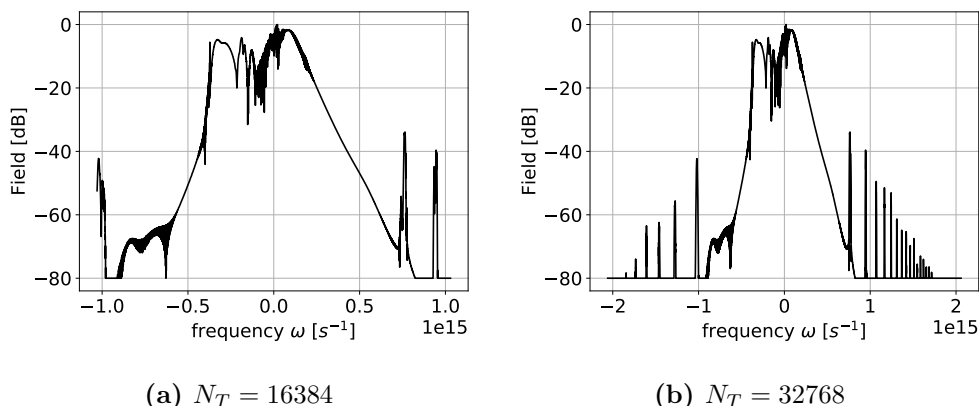


Figure 4.13: Spectra against ω for various number of samples N_T in the time-domain on a log scale. Here, N_T was chosen to accommodate the entire spectrum while minimizing computation time. In this case $N_T = 16384$. Furthermore, ω is the angular frequency relative to the carrier frequency ω_0 .

The number of computational steps N_z was taken as the least amount of steps, after which the spectrum of the pulse did not seem to depend on N_z anymore, i.e., after the spectrum had converged. In figure 4.14, we see for the spectrum of the same Gaussian pulse how the part of the spectrum that represents numerical artefacts disappears, while the physical part remains, as N_z is increased. A stable spectrum is obtained for $N_z \geq 32768$. This is again demonstrated in figure 4.14d, where we plot the relative difference δ between solutions as a function of the number of steps N_z . The relative difference has dropped to about 10^{-6} for the case of figure 4.14c, which does not show numerical artefacts. Note that figure 4.14c shows the relative difference between the solutions with N_z and $2N_z$.

To conclude, we have outlined a procedure a user of the code can use to determine optimal settings for the numerical parameters, i.e., for T_{\max} , N_T and N_z that provide a true-to-reality result, while minimising computational time. These numerical parameters strongly depend on the value of the physical parameters, such as peak power P_0 , pulse duration T_0 , nonlinear parameter γ and the dispersion considered, and should be re-evaluated whenever one of physical parameters changes. In general, stronger nonlinear optical processes require a higher resolution in the simulation to properly resolve all the features induced by the nonlinear processes.

4.2.5 Simulation of supercontinuum generation

Finally, we employ the approach described in section 4.2.4 to simulate the propagation of Gaussian pulses with a pulse width of $T_0 = 60$ fs for the cases seen in table 4.3. Note that the propagation distance z_{\max} is varied inversely with the peak power P_0 , since L_{NL} varies inversely with P_0 . In addition, the pulse energy

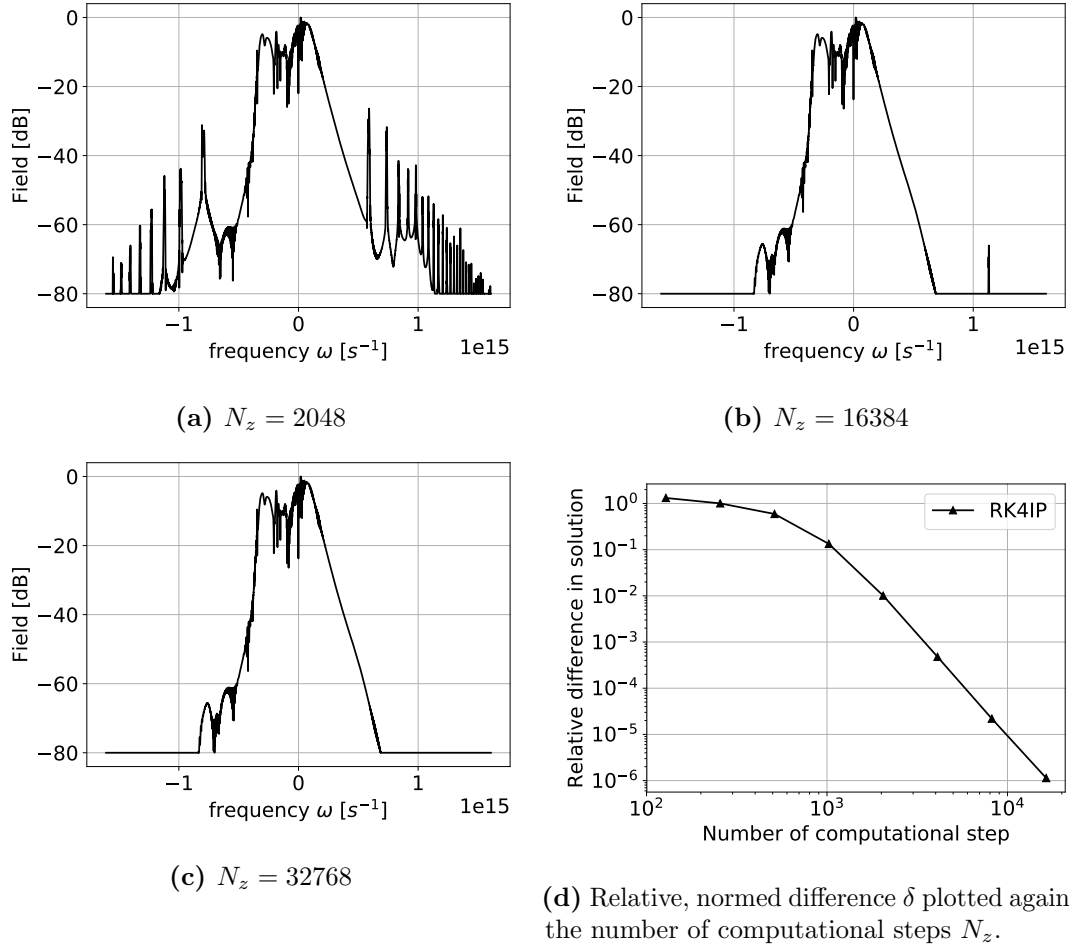


Figure 4.14: (a,b,c) Spectra of a Gaussian pulse, after propagating 6.73 m, on a logarithmic scale, calculated with varying number of computational steps. The plots show the reduction of numerical artefacts and reveal the physical part of the solution as N_z increases. Additionally, (d) shows a log-log plot of the relative difference δ between the solutions with N_z and $2N_z$, against the number of computational steps N_z . Again, ω is the angular frequency relative to the carrier frequency ω_0 .

P_0 [W]	N	Pulse energy [pJ]	z_{\max} [m]	Spectral width [THz]
Gaussian pulse, 1.0	0.464	0.0752	NA	27.9
1.0	0.464	0.0752	0.5	29.4
10.0	1.468	0.7520	20.0	49.7
100.0	4.641	7.5199	2.0	118.4
1044.60	15	75.553	0.2	269.6
4178.38	30	501.41	0.05	546.7

Table 4.3: Results from simulating SCG, obtained from figures 4.16 and 4.15. It lists the pulse peak powers P_0 , the equivalent soliton order N as in equation 4.1, the pulse energy and the spectral width of the resulting pulse at the -30 dB level for pulses with pulse width $T_0 = 60$ fs. The propagation length z_{\max} was scale inversely with P_0 , similarly to L_{NL} . For $P_0 = 1.0$ W, we found that the little change to the spectrum occurs before 0.5 m.

and spectral width of a Gaussian pulse with $P_0 = 1$ W has been added as a point of reference. For the first case, $P_0 = 1$ W, we observed a broadening in the time domain. When we look at figure 4.15a, we see a comparison of its spectrum after propagation with that of the initial Gaussian pulse. The figure shows that the spectrum has barely been altered. This indicates that, due to the low intensity, hardly any SPM occurred in the pulse, since SPM is the only nonlinear process that affects the pulse spectrum. Note that dispersive effects do not alter the spectrum of a pulse, since they are linear in nature, and we conclude that the temporal broadening was purely the effect of dispersion. Also note that for this pulse, $N < 1/2$, so no soliton formation can take place.

As the peak power increases for the next cases, so does the spectral width. This can be explained by noting that a Gaussian pulse forms into a soliton pulse for $N > 1/2$ during propagation. Then, for $N > 3/2$, the higher-order soliton splits into multiple fundamental solitons due to the process of soliton fission, according to the rules of equation 2.33. In this equation, we see that a higher N , and thus a higher peak power, leads to formation of narrower solitons. The width of the resulting spectrum depends on the spectral width of the resulting soliton with the widest spectrum, i.e., with the shortest pulse width. Recall that a more narrow pulse means a broader spectrum. Thus, higher peak power leads to a wider spectrum.

Furhtermore, if the spectral broadening solely depends on soliton fission, we expect the spectrum to stabilise once the fission process is complete. This is exactly what we observe in figure 4.16a for a pulse energy of 501.41 pJ, namely that the spectrum broadens extremely quickly in about 1.24 cm and then settles at a spectral width of 546.7 THz at the -30 dB level.

Figures 4.16b and 4.16a show that we have been able to successfully model extreme supercontinuum generation when a short, high energy pulse propagates through a photonic crystal fiber having anomalous dispersion. The simulations gives us access to both the pulse dynamics in the temporal and spectral domain, which helps us understanding the physics involved. The ultimate test would be to compare

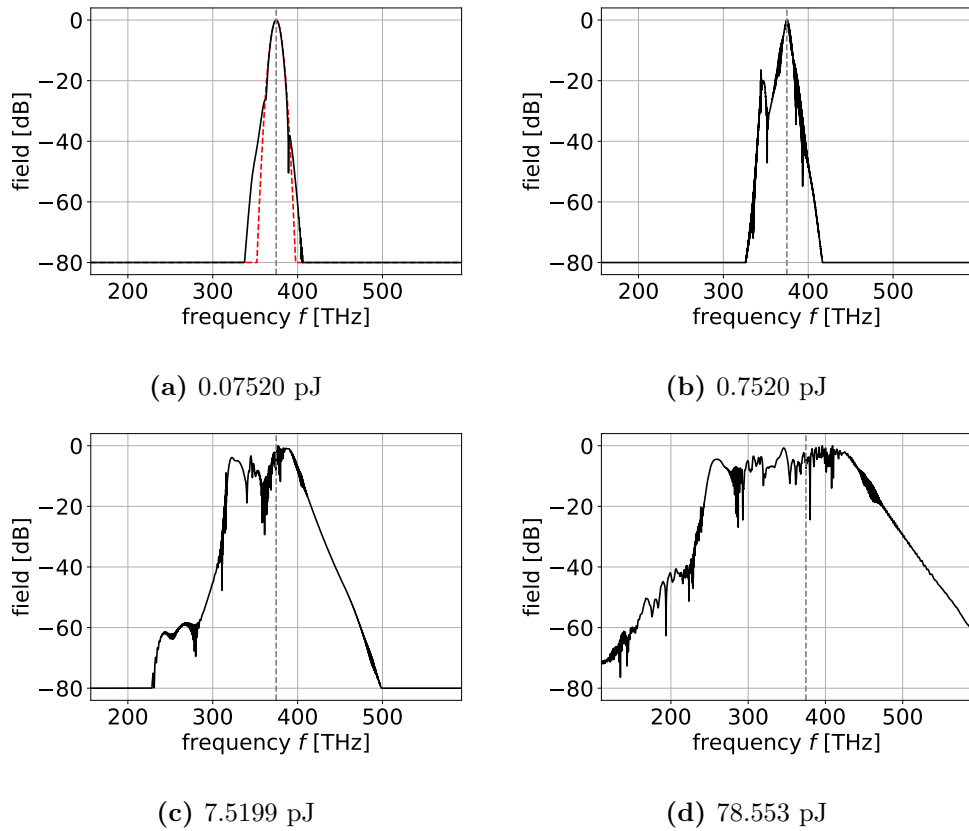


Figure 4.15: Spectrum of Gaussian pulses with pulse energies of 0.0752, 0.7520, 7.5199 and 78.553 pJ at $z = 0.5, 20, 2.0$ and 0.2 m, respectively, with a spectral widths of 29.4, 49.7, 118.4 and 296.6 THz. The vertical, dotted lines indicate $f_0 = 374.74$ THz. The red curve in (a) indicates the spectrum of the initial Gaussian pulse with a pulse energy of 0.0752 pJ and a spectral width of 27.9 THz.

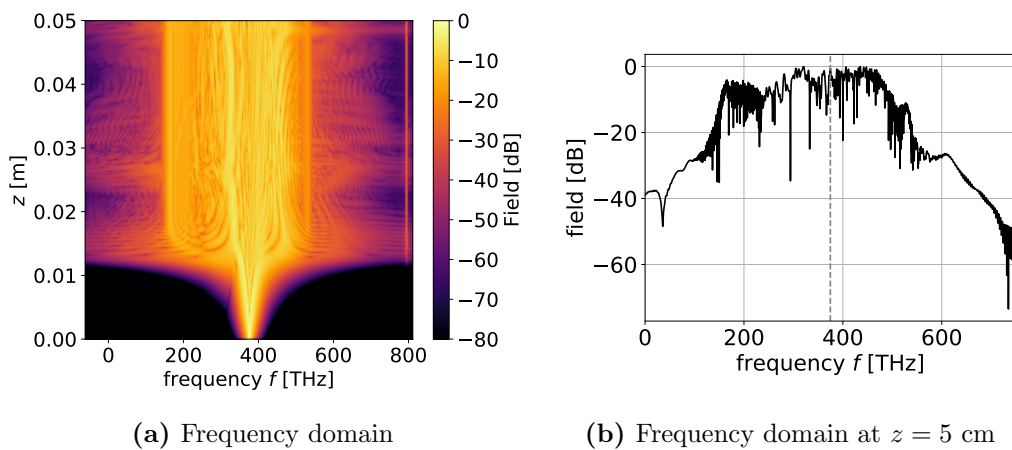


Figure 4.16: Spectrum of a Gaussian pulse with a pulse energy of 501.41 pJ for (a) propagation over $z \in (0, 0.05]$ m and for (b) $z = 5$ cm. It spans $f \in [82.8, 629.5]$ THz, with a spectral width of 546.7 THz. The vertical, dotted line in (b) indicates $f_0 = 374.74$ THz.

the numeric results with experimental results, however, this requires that a more complete description of the various nonlinear optical processes is included in the simulations. Implementation of the missing processes is foreseen in the near future. So far, the simulation code developed gives a promising start for studying the nonlinear propagation in various waveguide systems and allows engineering of the waveguides to optimise particular characteristics of the nonlinear propagation.

Chapter 5

Conclusions & outlook

The nonlinear propagation of optical pulses is described by the generalised nonlinear Schrödinger equation (GNLSE), which reduces to the nonlinear Schrödinger equation (NLSE) when dispersion is included up to group velocity dispersion and only the nonlinear third-order Kerr effect is included. We provided a summary of the derivation of the NLSE from Maxwell's equations, including the approximations and assumptions that were made, highlighting its limitations. The NLSE has analytic solutions known as solitons that are not only a major ingredient in supercontinuum generation (SCG), but also play an important role in validation of any simulation code that solves the (G)NLSE. We presented approximate, analytic solutions of the GNLSE that can be obtained under appropriate conditions and can be used for further validation. To solve both equations we described two pseudo-spectral methods known as the split-step Fourier method (SSFM) and the fourth-order Runge-Kutta method in the interaction picture (RK4IP). Moreover, we introduced a measure that can be used to verify the convergence of the numeric solution. We showed that this measure can be used to obtain the order of convergence, even in the absence of a reference solution. This measure is used to demonstrate 2nd- and 4th-order convergence for SSFM and RK4IP, respectively. Apart from having showed the appropriate order of convergence, our Python implementation of the two methods also correctly simulated fundamental and second-order soliton propagation when solving the NLSE. For the GNLSE, we showed the correct simulation of the drift of fundamental solitons in the presence of third-order dispersion and fission of higher-order solitons in the presence of higher-order dispersion, indicating that we have correctly implemented the two methods in our simulation code.

Having both verified and validated our newly developed code for simulating nonlinear pulse propagation in waveguides, we used it to develop insight into various physical processes that one cannot get from experimental or analytical results. We presented the results of simulating the propagation of non-integer solitons and a Gaussian pulse. We found that the prediction, that these pulses asymptotically converge to their closest integer soliton counterpart, is not as clear-cut as one might initially think. We hypothesised that renormalisation of the results w.r.t. their new peak power and pulse width is necessary for showing convergence to stable,

integer-order solitons. Additionally, we showed that the distance it takes for a pulse to converge to its asymptote depends on the difference between the pulse and the asymptote. After having given thought to the conditions for correctly choosing numerical parameters, we presented results for simulating the process of extreme broadening of Gaussian pulses, i.e., SCG. We showed the resulting spectra of Gaussian pulses with pulse energies up to 501 pJ, after soliton fission had occurred. For the highest pulse energy, we ended up with a supercontinuum with a spectral width of 547 THz at the -30 dB level. Although not all relevant, nonlinear processes have yet been included, having a simulation code available to model nonlinear propagation allows us to selectively turn certain physical processes on and off. Furthermore, we can retrieve information about the dynamics of the nonlinear propagation that cannot be experimentally accessed. Having such a tool available helps us to improve the engineering of waveguides for, among others, SCG.

5.1 Outlook

The development of the code, as described in this report, opens up a number of new challenges that form opportunities for new research in the future. As stated in the introduction of this report, one of our aims was to not only use the relatively new and highly promising RK4IP to simulate pulse propagation in straight waveguides, but apply this numerical method to microring resonators as well. So far, SSFM is the most commonly used method for this [43, 16]. Another step that can be made to extend the use of the code, is the inclusion of more physical effects from the GNLSE, such as loss, self-steepening, Raman scattering and spontaneous Raman noise [18]. Even though Raman scattering can be neglected for silicone nitride waveguides [22, 60], this may not be the case for all material platforms.

Computation time remains an obstacle when simulating the nonlinear propagation of pulses, especially for highly dynamic cases, e.g., for high pulse energies and when including more complicated processes, such as higher-order dispersion, self-steepening or Raman scattering. When simulating such cases, a high level of accuracy is required in order to correctly model all the features. Adaptive step-size methods can be implemented to increase the efficiency of both SSFM and RK4IP [8, 52]. Using adaptive step-size methods is especially effective when using RK4IP [33].

Finally, RK4IP was first presented in the PhD thesis of Caradoc-Davies [13]. In his thesis, Caradoc-Davies proposes an efficient method of implementing RK4IP in Python in appendix B.3. The implementation uses FFTW [24] to perform the FFTs, presumably in order to decrease computation time, and speeds up the method by implementing certain steps as C routines and performs operations in-place wherever possible to reduce memory requirements. Since Python has a strong integration with C, implementing routines inside of a Python program in C should be efficient and seamless. Since our code is already implemented in

Python, following the implementation proposed by Caradoc-Davies is a logical step that could improve performance. Alternatively, there exists an open-source code project that uses SSFM to simulate Kerr frequency comb generation [43]. This project again uses FFTW and Python and integrates this with a backend in Julia, a high-level, high-performance programming language designed for numerical analysis [2]. Taking inspiration from this open-source code project by implementing the solver of our code in Julia and integrating it within our Python environment might also help increase performance.

The ability of the solver to simulate SCG has been demonstrated in this report. Including the additions and improvements, as stated above, would both extend the use of the code, by including more physical effects, and increase its efficiency, allowing for more complex cases to be studied while keeping computational times manageable.

References

- [1] Python's NumPy module documentation. <https://numpy.org/doc/stable/>. Accessed: 29-08-2020.
- [2] Python's NumPy module documentation. <https://julialang.org/>. Accessed: 29-08-2020.
- [3] Python's `time` module documentation. <https://docs.python.org/3/library/time.html>. Accessed: 18-08-2020.
- [4] G. P. Agrawal. *Nonlinear Fibre Optics, 2nd Ed.* Academic Press, 5th edition, 2013.
- [5] N. Akhmediev and M. Karlsson. Cherenkov radiation emitted by solitons in optical fibers. *Physical Review A*, 51(3):2602–2607, 1995.
- [6] R. R. Alfano and S. L. Shapiro. Emission in the Region 4000 to 7000 Å via Four-Photon Coupling in Glass. *Physical Review Letters*, 24(11):584–587, Mar. 1970.
- [7] R. R. Alfano and S. L. Shapiro. Observation of Self-Phase Modulation and Small-Scale Filaments in Crystals and Glasses. *Physical Review Letters*, 24(11):592–594, Mar. 1970.
- [8] S. Balac and A. Fernandez. Comparison of adaptive step-size control strategies for solving the Generalised Non-Linear Schrodinger Equation in optics by the Interaction Picture method. *Optics Journal of Computational Physics*, 280:295–305, 2015.
- [9] C. Besse, B. Bidégaray, and S. Descombes. Order Estimates in Time of Splitting Methods for the Nonlinear Schrödinger Equation. *SIAM Journal on Numerical Analysis*, 40(1):26–40, 2002.
- [10] N. Bloembergen. Nonlinear optics: Past, present, and future. *IEEE Journal of Selected Topics in Quantum Electronics*, 6(6):876–880, Nov. 2000.
- [11] K. J. Blow and D. Wood. Theoretical description of transient stimulated Raman scattering in optical fibers. *IEEE Journal of Quantum Electronics*, 25(12):2665–2673, 1989.

- [12] R. W. Boyd. *Nonlinear Optics*. Academic Press, 2007.
- [13] B. M. Caradoc-Davies. *Vortex Dynamics in Bose-Einstein Condensates*. PhD thesis, University of Otago, Dunedin, New Zealand, 2000.
- [14] Q. Chang, E. Jia, and W. Sun. Difference Schemes for Solving the Generalized Nonlinear Schrödinger Equation. *Journal of Computational Physics*, 148(2):397–415, 1999.
- [15] Y. K. Chembo. Kerr optical frequency combs: Theory, applications and perspectives. *Nanophotonics*, 5(2), Jan. 2016.
- [16] S. Coen, H. G. Randle, T. Sylvestre, and M. Erkintalo. Modeling of octave-spanning Kerr frequency combs using a generalized mean-field Lugiato–Lefever model. *Optics Letters*, 38(1):37, 2013.
- [17] Cooley and Tukey. An Algorithm for the Machine Calculation of Complex Fourier Series. *Mathematics of Computation*, 19(90):6, 1965.
- [18] J. M. Dudley, G. Genty, and S. Coen. Supercontinuum generation in photonic crystal fiber. *Reviews of Modern Physics*, 78(4):1135–1184, Oct. 2006.
- [19] S. Dupont, C. Petersen, J. Thøgersen, C. Agger, O. Bang, and S. R. Keiding. IR microscopy utilizing intense supercontinuum light source. *Optics Express*, 20(5):4887, Feb. 2012.
- [20] P. Emplit, J. Hamaide, F. Reynaud, C. Froehly, and A. Barthelemy. Picosecond steps and dark pulses through nonlinear single mode fibers. *Optics Communications*, 62(6):374–379, 1987.
- [21] J. Epping. *Dispersion Engineering Silicon Nitride Waveguides for Broadband Nonlinear Frequency Conversion*. PhD thesis, University of Twente, Enschede, The Netherlands, 2015.
- [22] J. P. Epping, T. Hellwig, M. Hoekman, R. Mateman, A. Leinse, R. G. Heide-
man, A. van Rees, P. J. van der Slot, C. J. Lee, C. Fallnich, and K.-J. Boller. On-chip visible-to-infrared supercontinuum generation with more than 495 THz spectral bandwidth. *Optics Express*, 23(15):19596, 2015.
- [23] R. A. Fisher and W. K. Bischel. Numerical studies of the interplay between self-phase modulation and dispersion for intense plane-wave laser pulses. *Journal of Applied Physics*, 46(11):4921–4934, 1975.
- [24] M. Frigo and S. G. Johnson. FFTW user’s manual. *Massachusetts Institute of Technology*, 1999. See also <http://www.fftw.org/>.
- [25] C. S. Gardner, J. M. Greene, M. D. Kruskal, and R. M. Miura. Method for Solving the Korteweg-deVries Equation. *Physical Review Letters*, 19(19):1095–1097, Nov. 1967.

- [26] C. S. Gardner, J. M. Greene, M. D. Kruskal, and R. M. Miura. Korteweg-devries equation and generalizations. VI. methods for exact solution. *Communications on Pure and Applied Mathematics*, 27(1):97–133, Jan. 1974.
- [27] A. Gourlay. Some recent methods for the numerical solution of time-dependent partial differential equations. *Proceedings of the Royal Society of London. A. Mathematical and Physical Sciences*, 323(1553):219–235, 1971.
- [28] N. Granzow. Supercontinuum white light lasers: A review on technology and applications. In B. Zagar, P. Mazurek, M. Rosenberger, and P.-G. Dittrich, editors, *Photonics and Education in Measurement Science 2019*, page 49, Jena, Germany, Sept. 2019. SPIE.
- [29] H. Guo, C. Herkommer, A. Billat, D. Grassani, C. Zhang, M. H. P. Pfeiffer, W. Weng, C.-S. Brès, and T. J. Kippenberg. Mid-infrared frequency comb via coherent dispersive wave generation in silicon nitride nanophotonic waveguides. *Nature Photon*, 12(6):330–335, 2018.
- [30] M. Haelterman, S. Trillo, and S. Wabnitz. Dissipative modulation instability in a nonlinear dispersive ring cavity. *Optics communications*, 91(5-6):401–407, 1992.
- [31] R. Halir, Y. Okawachi, J. S. Levy, M. A. Foster, M. Lipson, and A. L. Gaeta. Ultrabroadband supercontinuum generation in a CMOS-compatible platform. *Optics Letters*, 37(10):1685, 2012.
- [32] T. W. Hänsch. Nobel Lecture: Passion for precision. *Reviews of Modern Physics*, 78(4):1297–1309, Nov. 2006.
- [33] A. Heidt. Efficient Adaptive Step Size Method for the Simulation of Supercontinuum Generation in Optical Fibers. *Journal of Lightwave Technology*, 27(18):3984–3991, 2009.
- [34] T. Herr. *Solitons and Dynamics of Frequency Comb Formation in Optical Microresonators*. PhD, École Polytechnique Fédérale de Lausanne, Lausanne, Switzerland, 2013.
- [35] T. Hohage and F. Schmidt. *On the Numerical Solution of Nonlinear Schrödinger Type Equations in Fiber Optics*. PhD thesis, Konrad-Zuse-Zentrum für Informationstechnik Berlin, Berlin-Dahlem, Germany, 2002.
- [36] J. Hult. A Fourth-Order Runge–Kutta in the Interaction Picture Method for Simulating Supercontinuum Generation in Optical Fibers. *Journal of Lightwave Technology*, 25(12):3770–3775, 2007.
- [37] A. V. Husakou and J. Herrmann. Supercontinuum Generation of Higher-Order Solitons by Fission in Photonic Crystal Fibers. *Physical Review Letters*, 87(20):203901, 2001.
- [38] K. Ikeda. Multiple-valued stationary state and its instability of the transmitted light by a ring cavity system. *Optics Communications*, 30(2):257–261, 1979.

- [39] P. Kelley. Self-focusing of optical beams. *Physical Review Letters*, 15(26):1005, 1965.
- [40] J. Kerr. A new relation between electricity and light: Dielectrified media birefringent. *The London, Edinburgh, and Dublin Philosophical Magazine and Journal of Science*, 50(332):337–348, 1875.
- [41] Y. Kivshar. Dark optical solitons: Physics and applications. *Physics Reports*, 298(2-3):81–197, 1998.
- [42] Y. Kodama and A. Hasegawa. Nonlinear pulse propagation in a monomode dielectric guide. *IEEE Journal of Quantum Electronics*, 23(5):510–524, 1987.
- [43] G. Moille, Q. Li, X. Lu, and K. Srinivasan. pyLLE: A Fast and User Friendly Lugiato-Lefever Equation Solver. *arXiv:1903.10441 [physics]*, Mar. 2019. See also <https://gregmoille.github.io/pyLLE/>.
- [44] D. Y. Oh, D. Sell, H. Lee, K. Y. Yang, S. A. Diddams, and K. J. Vahala. Supercontinuum generation in an on-chip silica waveguide. *Optics Letters*, 39(4):1046, Feb. 2014.
- [45] P. Parra-Rivas, E. Knobloch, D. Gomila, and L. Gelens. Dark solitons in the Lugiato-Lefever equation with normal dispersion. *Physical Review A*, 93(6):063839, 2016.
- [46] A. Pazy. *Semigroups of Linear Operators and Applications to Partial Differential Equations*. Springer-Verlag NewYork, Inc., 1983.
- [47] J. Pfeifle, A. Coillet, R. Henriët, K. Saleh, P. Schindler, C. Weimann, W. Freude, I. V. Balakireva, L. Larger, C. Koos, and Y. K. Chembo. Optimally Coherent Kerr Combs Generated with Crystalline Whispering Gallery Mode Resonators for Ultrahigh Capacity Fiber Communications. *Physical Review Letters*, 114(9):093902, Mar. 2015.
- [48] M. Ren, S. Yun, and Z. Li. Nonlinear conservation laws for the Schrödinger boundary value problems of second order. *Boundary Value Problems*, 2020(1):1, 2020.
- [49] J. Satsuma and N. Yajima. B. Initial Value Problems of One-Dimensional Self-Modulation of Nonlinear Waves in Dispersive Media. *Progress of Theoretical Physics Supplement*, 55:284–306, 1974.
- [50] A. Shabat and V. Zakharov. Exact theory of two-dimensional self-focusing and one-dimensional self-modulation of waves in nonlinear media. *Soviet physics JETP*, 34(1):62, 1972.
- [51] C. Shannon. Communication in the Presence of Noise. *Proceedings of the IRE*, 37(1):10–21, Jan. 1949.
- [52] O. Sinkin, R. Holzlohner, J. Zweck, and C. Menyuk. Optimization of the split-step fourier method in modeling optical-fiber communications systems. *Journal of Lightwave Technology*, 21(1):61–68, 2003.

- [53] G. Strang. On the construction and comparison of difference schemes. *SIAM Journal on Numerical Analysis*, 5(3):506–517, 1968.
- [54] M.-G. Suh, Q.-F. Yang, K. Y. Yang, X. Yi, and K. J. Vahala. Microresonator soliton dual-comb spectroscopy. *Science*, 354(6312):600–603, 2016.
- [55] T. R. Taha and M. I. Ablowitz. Analytical and numerical aspects of certain nonlinear evolution equations. II. Numerical, nonlinear Schrödinger equation. *Journal of Computational Physics*, 55(2):203–230, 1984.
- [56] G. H. Weiss and A. A. Maradudin. The Baker-Hausdorff Formula and a Problem in Crystal Physics. *Journal of Mathematical Physics*, 3(4):771–777, 1962.
- [57] G. Wilson, D. A. Aruliah, C. T. Brown, N. P. Chue Hong, M. Davis, R. T. Guy, S. H. D. Haddock, K. D. Huff, I. M. Mitchell, M. D. Plumbley, B. Waugh, E. P. White, and P. Wilson. Best Practices for Scientific Computing. *PLoS Biology*, 12(1):e1001745, Jan. 2014.
- [58] K. Wörhoff, R. G. Heideman, A. Leinse, and M. Hoekman. TriPleX: A versatile dielectric photonic platform. *Advanced Optical Technologies*, 4(2), Jan. 2015.
- [59] N. J. Zabusky and M. D. Kruskal. Interaction of "Solitons" in a Collisionless Plasma and the Recurrence of Initial States. *Physical Review Letters*, 15(6):240–243, Aug. 1965.
- [60] H. Zhao, B. Kuyken, S. Clemmen, F. Leo, A. Subramanian, A. Dhakal, P. Helin, S. Severi, E. Brainis, G. Roelkens, and R. Baets. Visible-to-near-infrared octave spanning supercontinuum generation in a silicon nitride waveguide. *Optics Letters*, 40(10):2177, 2015.

Appendix A

Modelling Kerr frequency comb generation

As mentioned in the introduction of this report, one of our goals was to apply RK4IP not only to the modelling of nonlinear pulse propagation in straight waveguides, but in microring resonators (MRRs) as well. This would allow our code to model Kerr frequency comb generation (KFCG), in addition to SCG. KFCG is similar to SCG, in that in both cases the spectrum of a pulse undergoes (extreme) broadening due to nonlinear processes. However, where the spectrum broadens continuously in a straight waveguide due to the interplay of dispersion and the nonlinear Kerr effect, only specific frequencies are allowed in a MRR, namely its resonance frequencies, resulting in a so-called Kerr frequency comb (KFC).

In this appendix, we present the Lugiato-Lefever equation (LLE), which describes the nonlinear propagation of light within a MRR. We treat some of its properties and show how SSFM and RK4IP can be used to solve it. Finally, we present our results of doing so for spatially uniform solutions as a first step of validating our implementation.

A.1 Lugiato-Lefever Equation

The process of KFCG consists of coupling a certain pump field E_{in} from a waveguide into a MRR, which is a ring-shaped waveguide (see figure A.1). When driven appropriately, the interplay between pump, dispersion and the Kerr effect can lead to soliton formation, and thus spectral broadening, within the MRR, which corresponds to a low-noise, highly coherent KFC. Thus, in addition to the nonlinear propagation inside the MRR, the model also needs to include coupling of light into and out of the MRR. The MRR is most easily modelled by considering a time window corresponding to the roundtrip time of the MRR, i.e., $\tau' \in [0, t_R)$, where t_R is the roundtrip time of the ring and τ' is the time indicating the position in

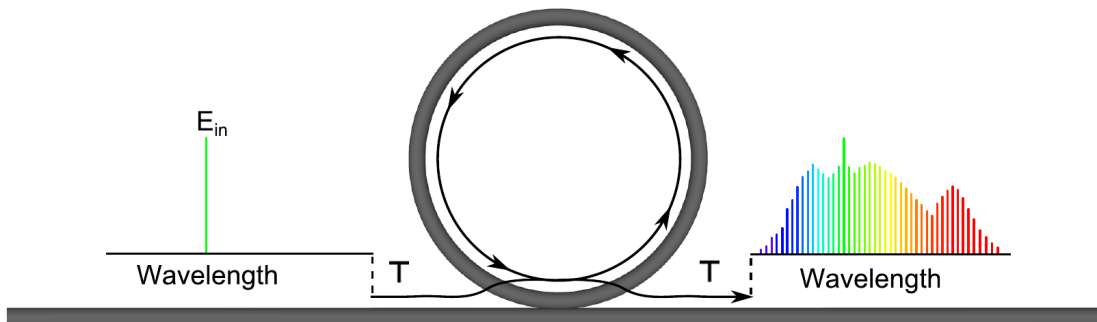


Figure A.1: Pump field E_{in} is coupled into and out of a ring resonator with coupling coefficient T , which gives rise to a Kerr frequency comb [16].

the ring. Further, periodic boundary conditions (PBCs) are to be applied, relating $E^{(m+1)}(0, \tau')$ at the beginning of the $(m+1)$ th roundtrip to $E^{(m)}(L, \tau')$ at the end of the m th roundtrip. The PBCs are given by [16]

$$E^{(m+1)}(z = 0, \tau') = \sqrt{T}E_{\text{in}} + \sqrt{1-T} E^{(m)}(z = L, \tau') \cdot e^{i\varphi_0}. \quad (\text{A.1})$$

Here, L is the roundtrip length of the ring, T is the power coupling coefficient between the input waveguide and the ring and φ_0 is the phase accumulated due to linear propagation over one roundtrip. These PBCs, combined with a form of the GNLSE, form a map that describes the effects on a pulse of making one roundtrip through the ring. Such a map is called an Ikeda map [30, 38]. For example, let's take the following form of the GNLSE, describing loss, higher-order dispersion and Kerr nonlinearity,

$$\partial_z E(z, \tau') = -\frac{\alpha_I}{2} E + i \sum_{k=2}^{\infty} \left[\frac{i^k}{k!} \beta_k \partial_{\tau'}^k \right] E + i\gamma |E|^2 E, \quad (\text{A.2})$$

where α_I is the intra-cavity field absorption coefficient of the ring. Assuming a high-finesse MRR and nonlinear and dispersion lengths that are much longer than the roundtrip length, the Ikeda map can be used to show that equations A.1 and A.2 can be averaged over the roundtrip length to yield the *Lugiato-Lefever equation* (LLE) [30],

$$t_R \cdot \partial_{t'} E(t', \tau') = -(\alpha_T + i\delta_0) E + iL \sum_{k=2}^{\infty} \left[\frac{i^k}{k!} \beta_k \partial_{\tau'}^k \right] E + i\gamma L |E|^2 E + \sqrt{T} E_{\text{in}}. \quad (\text{A.3})$$

Here, δ_0 is the detuning of E_{in} with the closest resonance frequency of the ring, $\alpha_T = (\alpha_I + T)/2$ is the total cavity loss and $t' := m \cdot t_R$ is the slow time of the ring, with m the roundtrip index [16]. The slow-time is limited to an integer times t_R , since equation A.3 is derived by averaging equation A.2 over the roundtrip length. Note that the spatial variable z in the GNLSE has been replaced by the temporal variable t' through the use of t_R . Equation A.3 is the equation we will be solving for $E^{(m)}(0, \tau') := E(t' = m \cdot t_R, \tau')$.

A.1.1 Dimensionless form

Just as was done with the NLSE in section 2.1.2, the LLE in equation A.3 can be written down in a normalised, dimensionless form for the case that only second-order dispersion is considered. In other words, only GVD is included while higher-order dispersion is neglected, i.e., $\beta_k = 0$ for all $k > 2$. Similar to the NLSE, normalising the LLE reduces the number of parameters, meaning that every set of parameters for the normalised LLE represents a whole class of systems that all behave similarly. The normalised form of the LLE is as follows [45]

$$\partial_t A(t, \tau) = -(1 + i\theta) A + i \operatorname{sgn}(\beta_2) \partial_\tau^2 A + i |A|^2 A + \rho, \quad (\text{A.4})$$

where $A(t, \tau) := E(t', \tau') \sqrt{\gamma L / \alpha}$, $t := \alpha t' / t_R$, $\tau := \tau' \sqrt{2\alpha / (L |\beta_2|)}$, $\rho := E_{\text{in}} \sqrt{\gamma L T / \alpha^3}$ and $\theta := \delta_0 / \alpha$. The parameter $\operatorname{sgn}(\beta_2)$ again distinguishes between normal and anomalous GVD, with $\operatorname{sgn}(\beta_2) = 1$ signifying normal and $\operatorname{sgn}(\beta_2) = -1$ anomalous GVD. So, where the non-normalised LLE depends on t_R , α_T , δ_0 , L , β_2 , γ , T and E_{in} (eight parameters), the normalised LLE depends only on the detuning θ , the pump strength ρ and the sign of the GVD $\operatorname{sgn}(\beta_2)$.

A.2 Steady state, spatially uniform solutions

Steady states of equation A.4 are solutions for which $\partial A(t, \tau) / \partial t = 0$, i.e., stable points in the nonlinear dynamics of the LLE. Of these steady states, the spatially uniform solutions are the simplest as they also obey $\partial A(t, \tau) / \partial \tau = 0$. Such solutions are constant solutions, i.e., $A(t, \tau) = A_0$. Inserting this uniform solution in equation A.4 yields a cubic polynomial

$$I_0^3 - 2\theta I_0^2 + (1 + \theta^2) I_0 = \rho^2, \quad (\text{A.5})$$

where $I_0 := |A_0|^2$ is the cavity power. Now, an interesting property of equation A.5 is that it has one solution I_0 for every ρ when $\theta < \sqrt{3} \approx 1.73$. However, when $\theta > \sqrt{3}$, there is a region in which every ρ has three solutions. These two cases are visualised in figure A.2, where we see I_0 plotted against ρ , once for $\theta = 1.4 < \sqrt{3}$ and once for $\theta = 2.0 > \sqrt{3}$ [45].

When there are multiple solution to equation A.5 for a certain ρ , the stable point to which the system will converge depends on its spatially uniform initial condition, i.e., $A(t = 0)$. This effect is also known as hysteresis. This can intuitively be understood by looking at figure A.2b. The stable, or steady state, cavity power I_0 , will vary, if possible, continuously with ρ . In other words, the stable points 'walk' along the solid lines as ρ changes. When one of the transition points at the end of a solid line is reached, the stable point will discontinuously transition to the next solid line. This means that the dashed lines can only be reached by introducing them as an initial condition, which is physically not possible.

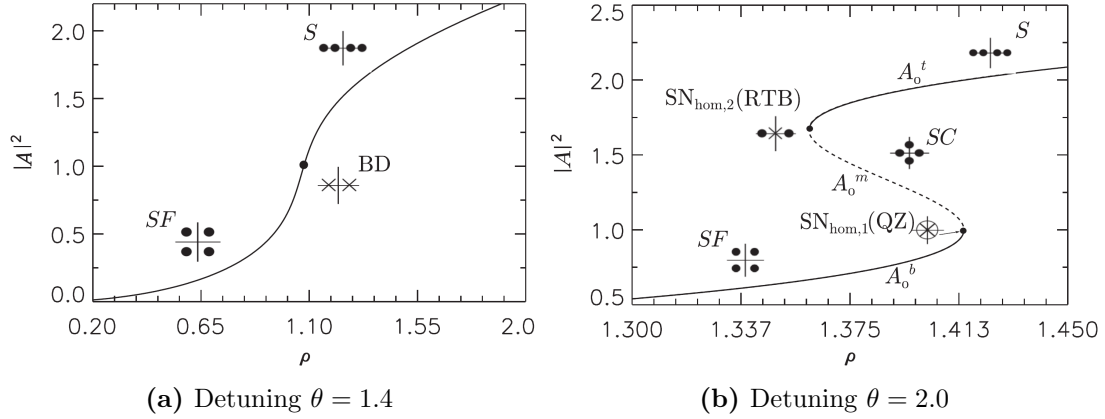


Figure A.2: Spatially uniform stable points of the LLE. The curves represent solutions to equation A.5, i.e., $|A|^2 = I_0$, for various values of ρ . In (a), we see there is one solution for every ρ , but in (b), we see there are three possible solutions for $\rho \in [1.360, 1.413]$. The solid lines represent the paths along which stable points 'walk' as ρ changes, the dashed lines represent stable points that cannot be reached physically [45].

Examples of this can be seen in figure A.3. This figure was obtained by solving equation A.4 for various spatially uniform initial conditions using RK4IP, for various values of ρ and θ . In figure A.3a, we see an exact copy of figure A.2a. In figure A.3b, we observe the expected hysteresis, in that the stable points to which the system converges depend on the initial condition $A(t = 0)$. Furthermore, we observe the discontinuous transition after passing a transition point. The transition points lie at $\rho = 1.413$ for the ascending and at for $\rho = 1.360$ for descending case, which agrees with figure A.2b. As ρ passes a transition point, the closer ρ remains to that transition point, the longer it takes for the solution to converge to the stable point. This means that a larger t_{\max} is required in those cases to converge to the stable point.

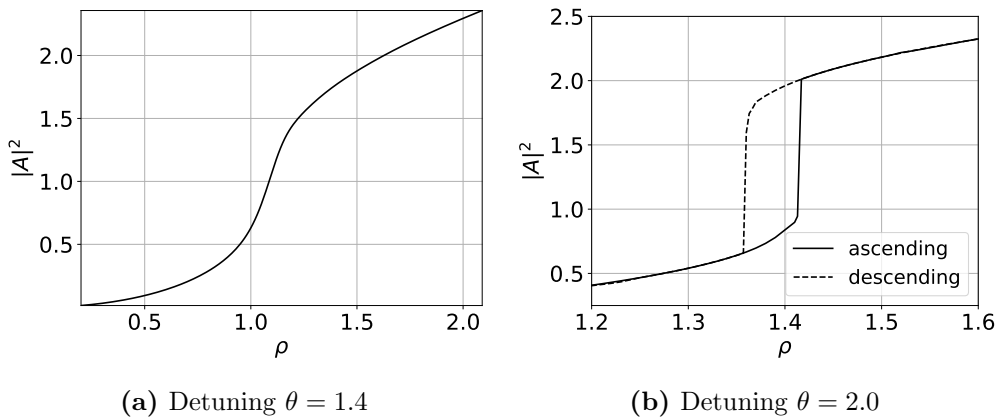


Figure A.3: Equilibrium cavity power $|A|^2$ vs. pump power ρ of spatially uniform solutions. In (a), no hysteresis can be seen, while in (b), a difference is observed between $|A(t = 0)|^2 = 0$ (ascending) and $|A(t = 0)|^2 = 2.5$ (descending), i.e., hysteresis.

Figure A.3 can be produced using either SSFM or RK4IP, where again RK4IP is the faster method to obtain a particular accuracy of the solution. Both methods show good agreement with the theoretical solutions of equation A.5. While the spatially uniform steady state solutions are used to validate the numerical implementation of the two methods, they do not show the interesting dynamics such as soliton formation and KFCG. For this, a spatial non-uniformity is required, such as a non-constant initial condition or noise, e.g., quantum fluctuations or spontaneous Raman fluctuations. See equation 2.28 for the inclusion of Raman fluctuations in the GNLSE. These fluctuations enable self-phase modulation, which leads to modulation instability and soliton formation in case of anomalous dispersion, as discussed in section 2.1.3, under appropriate driving conditions. An approximate analytical solution to the LLE for a soliton on a background field is available [34, appendix C]. Simulating this is a work in progress.